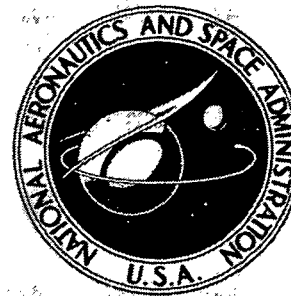


NASA CONTRACTOR
REPORT

NASA CR-2154



NASA CR-2154

INTERACTION OF THE SPACE SHUTTLE
CONTROL SYSTEM WITH POGO

by *A. Stewart Hopkins and William F. Davis*

Prepared by

MCDONNELL DOUGLAS ASTRONAUTICS COMPANY

Huntington Beach, Calif. 92647

for Langley Research Center

NATIONAL AERONAUTICS AND SPACE ADMINISTRATION • WASHINGTON, D. C. • DECEMBER 1972

1. Report No. NASA CR-2154	2. Government Accession No.	3. Recipient's Catalog No.	
4. Title and Subtitle INTERACTION OF THE SPACE SHUTTLE CONTROL SYSTEM WITH POGO		5. Report Date December 1972	
		6. Performing Organization Code	
7. Author(s) A. Stewart Hopkins and William F. Davis		8. Performing Organization Report No. MDC G2961	
9. Performing Organization Name and Address McDonnell Douglas Astronautics Company Huntington Beach, California		10. Work Unit No.	
		11. Contract or Grant No. NAS1-11055	
12. Sponsoring Agency Name and Address National Aeronautics and Space Administration Washington, D.C. 20546		13. Type of Report and Period Covered Contractor Report	
		14. Sponsoring Agency Code	
15. Supplementary Notes			
16. Abstract The asymmetric configuration of the Space Shuttle results in coupled pitch and axial vibration modes. This coupling results in interaction between the pogo and control systems. A detailed model of representative Space Shuttle structure, feedline, control, and engine systems revealed the coupled system may be unstable even though the pogo and control systems are stable individually. A method is developed for predicting the coupled system stability in terms of the stability of the separate systems.			
17. Key Words (Suggested by Author(s)) Asymmetry Control System Coupled Modes Interaction		18. Distribution Statement Pogo Space Shuttle System Stability	
19. Security Classification (of this report) Unclassified	20. Security Classification (of this page) Unclassified	21. No. of Pages 67	22. Price* \$3.00

*For sale by the National Technical Information Service, Springfield, Virginia 22151

CONTENTS

	Page
SUMMARY	1
INTRODUCTION	2
SYMBOLS	4
ANALYTICAL MODELS	9
Structure	10
Feedline	19
Control	26
Engine	29
Coupled System	32
STABILITY INVESTIGATION	39
Method	40
Baseline	41
Sensitivity	43
Interaction	57
CONCLUSIONS	62

INTERACTION OF THE SPACE SHUTTLE

CONTROL SYSTEM WITH POGO

By A. Stewart Hopkins and William F. Davis
McDonnell Douglas Astronautics Company

SUMMARY

Pogo and control instabilities have been of major concern in the design of aerospace vehicles; however, the symmetry of past vehicles and the associated absence of axial-lateral coupling have precluded the interaction of the pogo and control systems.

Currently proposed Space Shuttle Systems consist of an orbiter riding in parallel with various combinations of propellant tanks and boosters. These asymmetric configurations result in coupled axial and pitch modes of vibration. The pogo system, sensitive to axial motion, and the control system, sensitive to pitch motion, will interact because of the coupled modes. To investigate this phenomenon, detailed models of a representative Space Shuttle structure and the associated feedline, control, and engine systems were acquired or developed. A model generated by coupling the subsystems in an appropriate manner was evaluated for stability by calculation of the complex eigenvalues. Eigenvalues of the coupled system were compared with those of systems with the engine or control system inactive. It was determined that even though a vehicle is stable with respect to both the pogo and control systems individually, the coupled system may have a strong instability. To allow the traditional independent analysis and design of the pogo and control systems, a method was developed for determining the stability of the coupled system in terms of the stability of the pogo and control systems separately. Although the method becomes imprecise for the case of very close roots, a simple extension provides upper and lower bounds for the stability.

INTRODUCTION

Oscillations due to coupled propulsion-structure instabilities, pogo, and control-structure instabilities have been experienced on numerous aerospace vehicles. The source of the pogo instability may be envisioned as follows. Propellant oscillations induced by axial structural oscillations produce variations in engine inlet pressure and propellant flow. These result in thrust perturbations which reinforce the structural motion. Similarly, control signal oscillations, induced by lateral structural oscillations, produce control forces which reinforce the structural motion. The axial and lateral modes are almost entirely uncoupled for traditional axisymmetric vehicles. Methods have been developed to evaluate pogo stability with respect to axial modes and control stability with respect to lateral modes. Requirements will exist to ensure the stability of the Space Shuttle in this conventional sense.

The Space Shuttle configuration, however, introduces the possibility of a new type of instability produced by pogo-control interaction. Currently proposed Space Shuttle Systems, such as illustrated in fig. 1, exhibit a high degree of asymmetry, which results from coupling an orbiter with various combinations of boosters and propellant tanks. As has been confirmed by preliminary analysis, the structural asymmetry results in strongly coupled axial and lateral modes. Structural oscillations, therefore, induce responses in both the propulsion and control systems. Additionally, the long lateral feedlines characteristic of many Space Shuttle designs allow propellant oscillations to be induced by lateral structural motion. The combined regenerative forces may be of substantially greater magnitude and different phase, introducing the possibility of instabilities that would not be predicted by conventional methods.

Although the study conclusions are relevant to any Space Shuttle configuration exhibiting structural asymmetry with attendant axial-lateral coupling or lateral feedline runs, the McDonnell Douglas Corporation (MDC) "recommended Phase B fully reusable baseline configuration" was selected for detailed analysis. This representative configuration was selected so the existing structural idealization, control and engine system models, and feedline design could be utilized. Analysis was limited to the pitch plane since symmetry precludes coupling with the remaining degrees of freedom, and to the LOX line because the fuel feedline runs are relatively short and the engine is insensitive to fuel side perturbations. The coupled system model was developed to accurately reflect the system behavior from 0.07 to 7 Hz. This includes the dominant frequency ranges of the control system (0.2 to 3 Hz), engine system (0.1 Hz and up), and the fundamental feedline and structural modes (0.7 to 7 Hz).

The purpose of this study was to determine the nature of the pogo-control system interaction and to develop evaluative stability analysis techniques. The stability of the coupled system was evaluated with closed-loop analysis procedures. These methods were found to be substantially more effective than open-loop or time-domain procedures. After the stability of a baseline configuration was evaluated at selected burn times, the period of maximum control participation, 25 percent burn, was selected for evaluating sensitivity to parametric variations of the structural, feedline, control, and engine systems.



Figure 1. Space Shuttle Configuration

SYMBOLS

A	control conditioned pitch rate
a	real part of system eigenvalue
A_E	area of feedline at engine
A_F	area of feedline segment
A_{FT}	area of feedline at tank
A_G	area of tank at liquid surface
A_R	effective area ratio defined in equation (4)
B	control conditioned attitude error
b	imaginary part of system eigenvalue
C	control command signal
C_{L_α}	aerodynamic lift coefficient gradient
D	coupled system damping matrix
d	feedline segment diameter
D_C	control system damping matrix
D_{EE}	engine system damping matrix
D_S	structure-feedline damping matrix
D_{SS}	augmented structure damping matrix partition
E	feedline wall Young's modulus
F_A	actuator force
F_C	control force
F_L	aerodynamic lift force

F_{XG}	axial force at gimbal
F_{ZG}	lateral force at gimbal
$F_{\theta G}$	moment at gimbal
g	acceleration of gravity
H_F	feedline modal force vector
h_L	height of liquid surface above center of mass
H_S	structure modal force vector
I	identity matrix
i	$\sqrt{-1}$
I_E	engine moment of inertia $\times 12$
IC	interaction coefficient
K	coupled system stiffness matrix
K_A	aerodynamic spring defined in equation (2)
K_C	control system stiffness matrix
K_{EE}	engine system stiffness matrix
$K_{\alpha\beta}$	$\alpha, \beta = R$ (for reaction), C (for cavitation), RC (for both reaction and cavitation), and F (for free); feedline stiffness matrix partitions defined by equations (10) and (11)
K_S	structure-feedline stiffness matrix
K_{SS}	augmented structure stiffness matrix partition
K_U	ullage spring rate
K_θ	control attitude gain
$K_{\dot{\theta}}$	control attitude rate gain
L	feedline segment length
l	center of pressure to center of mass distance
M	coupled system mass matrix
M_A	actuator moment

M_C	control system mass matrix
M_E	engine mass x 12
M_{EE}	engine system mass matrix
M_{FF}	feedline mass matrix partition
<hr/>	
M_L	tank fluid mass
$M_{L\alpha\beta}$	$\alpha, \beta = S$ (for structure), F (for fluid); structure-tank mass matrix partitions defined by equation (6)
M_R	mass flow from tank
M_S	structure-feedline mass matrix
M_{SL}	slosh mass
$M_{\alpha\beta}$	$\alpha, \beta = S$ (for structure), T (for tank fluid); augmented structure mass matrix partitions defined by equations (7) and (8)
M_∞	Mach number
P_G	ullage gas pressure
P_S	suction pressure at engine inlet
P_T	pressure at tank sump
q	dynamic pressure
Q_C	engine fluid inertial force
q_C	engine fluid inertial displacement
Q_F	feedline force vector
q_F	feedline displacement vector
Q_{FT}	feedline force at tank
q_{FT}	feedline displacement at tank
q_L	total displacement tank fluid center of mass
Q_R	feedline reaction force vector
q_R	feedline reaction displacement vector
Q_{RC}	vector whose partitions are Q_R and Q_C defined by equation (11)

q_{RC}	vector whose partitions are q_R and q_C defined by equation (11)
q_{RE}	vector whose partitions are q_R and X_E defined by equation (12)
Q_S	augmented structure force vector
q_S	augmented structure displacement vector
q_{SL}	slosh generalized displacement
s	Laplace operator
S_{REF}	aerodynamic reference area
T	engine thrust x 12
t	feedline wall thickness
V_G	tank ullage gas volume
V_L	tank fluid volume
\dot{W}	weight flow through engine
X	global state vector
X_E	engine axial displacement
X_L	displacement structural tank mode
X_R	tank fluid center of mass motion due to flow
X_T	axial displacement of tank bottom
Z_E	lateral displacement at engine center of mass
Z_G	lateral displacement at gimbal
α	aerodynamic angle of attack
β	LOX bulk modulus
χ	control gain parameter
δ	engine gimbal angle
ϵ	control frequency parameter
η_F	feedline modal amplitude vector
η_S	structure modal amplitude vector

γ_G	ullage gas specific heat ratio
λ	gimbal to engine center of mass distance
μ	metric scale factor
ω	system natural frequency
ω_A	aerodynamic frequency
ω_F	feedline frequency diagonal matrix
ω_S	structural frequency diagonal matrix
ω_{SL}	slosh frequency
ϕ_F	feedline mode shape matrix
ϕ_{SARU}^T	vector of structure rotational mode shapes at attitude reference unit
ϕ_{SR}	structure mode shape matrix at reaction coordinates
ϕ_{SRC}	structure mode shape matrix at reaction coordinates and engine
ϕ_{SRG}^T	vector of structure rotational mode shapes at rate gyro
ϕ_{SXG}^T	vector of structure axial mode shapes at gimbal
ϕ_{SZG}^T	vector of structure lateral mode shapes at gimbal
ϕ_{SEG}^T	vector of structure rotational mode shapes at gimbal
ϕ_{XL}^T	vector of structure mode shapes for fluid tank mode
ϕ_{XT}^T	vector of structure mode shapes at tank bottom
$\phi_{Z,2}$	lateral mode shape in rigid-body plunge
ϕ_{ZT}^T	vector of structure lateral mode shapes at tank bottom
$\phi_{\theta,3}$	rotational mode shape in rigid-body pitch

ρ	LOX mass density
θ_{ARU}	pitch rotation at attitude reference unit
θ_E	engine rotation
θ_G	rotation at gimbal
θ_{RG}	pitch rotation at rate gyro
ζ	system fraction of critical damping
ζ_A	aerodynamic fraction of critical damping
ζ_C	system fraction of critical damping, control only
ζ_F	feedline fraction of critical damping diagonal matrix
ζ_P	system fraction of critical damping, pogo only
ζ_{PC}	system fraction of critical damping, pogo and control
ζ_S	structure fraction of critical damping diagonal matrix
ζ_{SL}	slosh fraction of critical damping
ζ_O	system fraction of critical damping, neither pogo nor control active

ANALYTICAL MODELS

To investigate the interaction of the pogo and control systems, the representative Phase B fully reusable baseline configuration was modeled in detail. The total system model was a composite of structural, fluid, control, and engine system analytical models.

The available structural model (representing a somewhat shorter version of the Shuttle) was scaled to the baseline configuration length, aerodynamic and slosh effects were incorporated, and fluid motion into the tank was added to facilitate coupling to the top of the feedline. The feedline model was developed from the feedline design and includes structural coordinates at bends for coupling to the structure, and weight flow for coupling to the engine model. Springs were incorporated to reflect pump cavitation and the design accumulator. The Phase B baseline control system was incorporated, including inertial effects of the gimbaled engine. A preliminary analytical engine model was obtained from an engine manufacturer. These four analytical models

were incorporated in a composite model by transforming each to a common set of variables and applying the appropriate compatibility and equilibrium relationships. The common set of variables includes pressures and flow as well as displacements and is therefore called a state vector.

Structure

The structural model was generated by making three enhancements to the available Phase B baseline idealization. Certain aerodynamic effects were included because of their potential effect on the control system. A slosh mode was added, also because of potential effect on the control system. Relative motion of fluid through the tank sump was introduced to facilitate later coupling with the feedlines.

The structural idealization used in this study was developed during the Phase B Space Shuttle study by McDonnell Douglas Astronautics Company-East for booster Configuration 14 and high cross-range Orbiter 0050. The lumped mass and beam element idealization used is illustrated in fig. 2. Three degrees of freedom, axial, plunge, and pitch rotation were allowed at each mass. The fluid mass in each tank was elastically connected to the tank aft bulkhead so that its frequency corresponded to the first tank mode frequency predicted by a simplified hydroelastic model. The Phase B fully reusable baseline configuration, booster Model 256-20B, is illustrated in fig. 3. The existing data were extrapolated to the baseline design by scaling the Model 14 length approximately 15 percent to make it conform with the Model 20B length. Natural frequencies and modal deflections remained unaltered. The natural frequencies for the model are presented in table 1. Modal damping of one percent was assumed for all modes, and all modes were mass normalized. Rigid-body axial, plunge, and pitch rotation modes were generated based on the mass properties generated during Phase B studies.

The aerodynamic force at the center of pressure was determined from the relationship:

$$F_L = S_{REF} q C_{L\alpha}(M_\infty) \alpha \quad (1)$$

where F_L is the aerodynamic lift force, S_{REF} is the reference area, q is the dynamic pressure, $C_{L\alpha}$ is the lift coefficient gradient, M_∞ is the Mach number, and α is the pitch angle of attack. Numerical values for these parameters, and the location of the center of pressure were generated during Phase B studies. Aerodynamic damping forces associated with pitch rate ranged from 0.03 to 11.0 percent of critical damping. The fraction of critical damping was conservatively set at 0.01 percent, $\zeta_A = 0.0001$. No other aerodynamic forces were considered relevant to the study. The aerodynamic forces of equation (1) are incorporated in the mathematical model as additions to the rigid-body partition (upper left) of the damping and stiffness matrices;

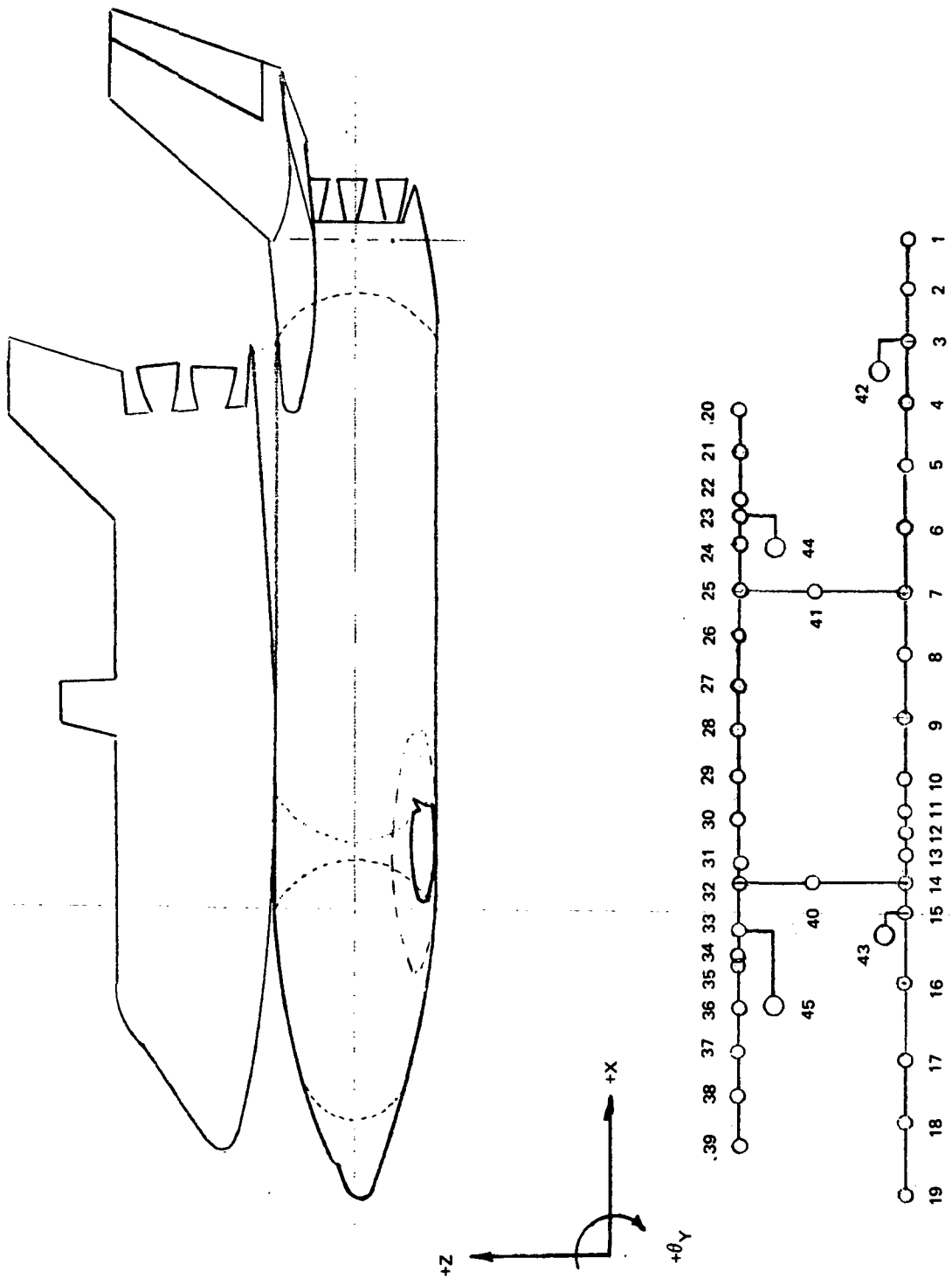


Figure 2. Space Shuttle Structural Idealization

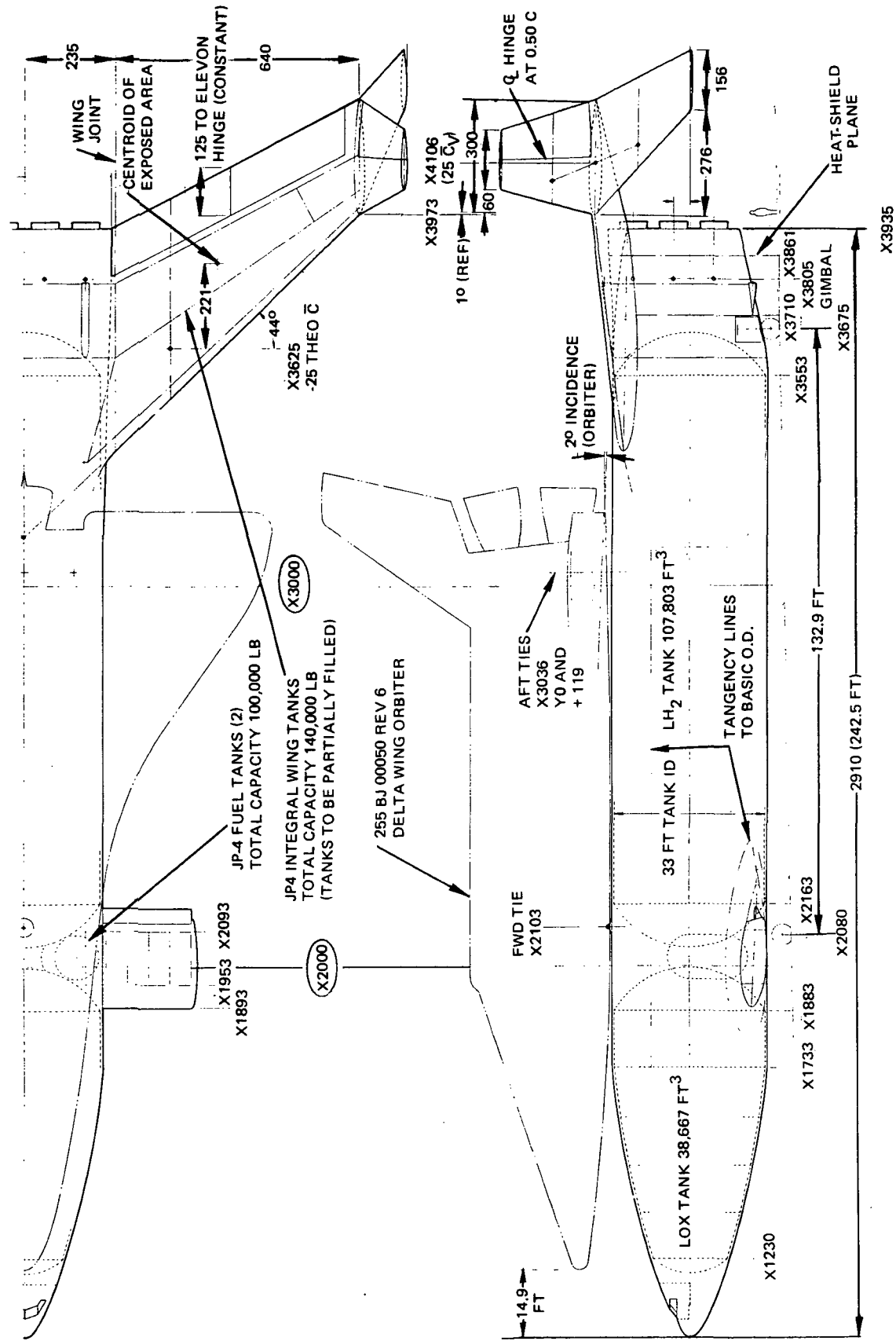


Figure 3. Space Shuttle Phase B Baseline Configuration

TABLE 1. NATURAL FREQUENCIES OF SPACE SHUTTLE STRUCTURE

Mode Number *	Frequency (Hz)			
	L/O	25% Burn	50% Burn	75% Burn
S4	0. 9083	0. 9456	0. 9859	1. 0453
S5	1. 3814	1. 5283	1. 6683	1. 8751
S6	2. 1490	2. 3259	2. 5427	2. 7729
S7	2. 6973	3. 2061	3. 8171	3. 9147
S8	3. 4052	3. 7391	3. 9050	4. 2108
S9	3. 8008	3. 9172	4. 3815	5. 1790
S10	4. 1991	4. 5451	4. 9540	6. 0467
S11	4. 5945	5. 1957	6. 4445	7. 0036
S12	6. 9202	6. 9755	6. 9980	7. 9997
S13	7. 2343	7. 6492	8. 1754	8. 7118

*Rigid-body axial, plunge, and pitch rotation structural modes (S1, S2, S3) omitted

$$\begin{bmatrix} 0 & 0 & 0 \\ 0 & 0 & 0 \\ 0 & 0 & 2\zeta_A \omega_A \end{bmatrix} \quad \left\{ \begin{array}{l} \eta_{S,1} \\ \eta_{S,2} \\ \eta_{S,3} \end{array} \right\}$$

and

$$\begin{bmatrix} 0 & 0 & 0 \\ 0 & 0 & K_A \\ 0 & 0 & \omega_A^2 \end{bmatrix} \quad \left\{ \begin{array}{l} \eta_{S,1} \\ \eta_{S,2} \\ \eta_{S,3} \end{array} \right\}$$

where

$$\omega_A^2 = \phi_{\theta,3}^2 \frac{F_L}{\alpha} \ell$$

and

$$K_A = -\phi_{\theta,3} \phi_{Z,2} \frac{F_L}{\alpha} \quad (2)$$

and where $\eta_{S,1}$, $\eta_{S,2}$, $\eta_{S,3}$ are the rigid-body axial, plunge, and pitch modal amplitudes; $\phi_{Z,2}$, $\phi_{\theta,3}$ are the plunge and pitch deflections of the rigid-body plunge and pitch mode shapes, and ℓ is the magnitude of the distance from center of mass to the center of pressure.

An attempt was made to incorporate slosh mass because of potential control system coupling. Only the booster LOX slosh mass was incorporated since it is much larger than the LH₂ or orbiter slosh masses. It can be shown that the addition of a relative slosh degree of freedom, q_{SL} , can be accomplished by augmenting the structural equations as follows:

$$\begin{aligned} & \left[\begin{array}{c|c} 0 & \sqrt{M_{SL}} \phi_{ZT}^T \\ \hline -\sqrt{M_{SL}} \phi_{ZT} & 1 \end{array} \right] \begin{Bmatrix} \dot{\eta}_S \\ q_{SL} \end{Bmatrix} \\ & + \left[\begin{array}{c|c} 0 & 0 \\ \hline 0 & 2\zeta_{SL}\omega_{SL} \end{array} \right] \begin{Bmatrix} \dot{\eta}_S \\ q_{SL} \end{Bmatrix} \\ & + \left[\begin{array}{c|c} 0 & 0 \\ \hline 0 & \omega_{SL}^2 \end{array} \right] \begin{Bmatrix} \dot{\eta}_S \\ q_{SL} \end{Bmatrix} = \begin{Bmatrix} 0 \\ 0 \end{Bmatrix} \quad (3) \end{aligned}$$

where M_{SL} is the slosh mass, ζ_{SL} is the slosh fraction of critical damping, ω_{SL} is the slosh frequency, η_S is the structure modal amplitudes, and ϕ_{ZT} is the lateral structural mode shapes at the attach point. Slosh parameters were generated during Phase B studies. The slosh mass was attached at the bottom of the LOX tank since mode shapes at that point were already being used for feedline coupling. This choice of attach point led to a minor control instability. For reasons discussed in the baseline stability investigation section, slosh was omitted in subsequent runs.

The structural modes as provided assumed no fluid motion out of the LOX tank; it was added since coupling the feedlines required that degree of freedom. The displacement of the tank mode degree of freedom, X_L , is approximately the same as the motion of the fluid center of mass (c. m.) with no flow. The total motion of the c. m., q_L , is the sum of the tank mode motion and an additional motion of the fluid c. m. due to a small flow out of the tank, X_R . For small relative flow, these relationships have the form:

$$q_L = X_L + X_R$$

where

$$X_R = \frac{M_R}{M_L} h_L = \frac{2 A_{FT} \rho h_L (q_{FT} - X_T)}{\rho V_L} = A_R (q_{FT} - X_T)$$

so

$$q_L = X_L + A_R (q_{FT} - X_T)$$

or

$$q_L = (\phi_{XL} - A_R \phi_{XT}) \eta_S + A_R q_{FT} \quad (4)$$

where M_R is the relative mass flow, M_L is the LOX tank fluid mass, h_L is the distance from the c.m. to liquid surface, $2 A_{FT}$ is the area of the two feedlines, ρ is the density, V_L is the LOX tank volume, q_{FT} is the fluid displacement at the top of the feedline, X_T is the axial displacement at the tank bottom, A_R is an effective area ratio defined by the equation, and ϕ_{XL} , ϕ_{XT} are the axial structural mode shapes of the tank mode, and the tank bottom degrees of freedom. The tank fluid mass is removed from the structural coordinate and added to the total motion coordinate, and the spring due to ullage gas, K_U , is added. The structural equations are augmented as follows:

$$\begin{bmatrix} -M_L & | & 0 \\ 0 & | & M_L \end{bmatrix} \begin{Bmatrix} \ddot{X}_L \\ q_L \end{Bmatrix} + \begin{bmatrix} K_U & | & -K_U \\ -K_U & | & K_U \end{bmatrix} \begin{Bmatrix} X_L \\ q_L \end{Bmatrix}$$

where

$$K_U = \frac{\gamma_G P_G A_G^2}{V_G}$$

Expressing q_L in terms of X_L , q_{FT} and X_T yields:

$$\begin{bmatrix} M_L A_R^2 & -M_L A_R & -M_L A_R^2 \\ -M_L A_R & 0 & M_L A_R \\ -M_L A_R^2 & M_L A_R & M_L A_R^2 \end{bmatrix} \begin{Bmatrix} X_T \\ X_L \\ q_{FT} \end{Bmatrix}$$

$$+ \begin{bmatrix} K_U A_R^2 & 0 & -K_U A_R^2 \\ 0 & 0 & 0 \\ -K_U A_R^2 & 0 & K_U A_R^2 \end{bmatrix} \begin{Bmatrix} X_T \\ X_L \\ q_{FT} \end{Bmatrix} = \begin{Bmatrix} 0 \\ 0 \\ Q_{FT} \end{Bmatrix} \quad (5)$$

where Q_{FT} is the associated force, γ_G is the gas specific heat ratio, P_G the ullage gas pressure, A_G the tank area at the liquid surface, and V_G the ullage gas volume. Comparison of the stiffness additions, $K_U A_R^2$, with the accumulator and other system stiffnesses showed them to be two orders of magnitude smaller. Since the springs are effectively parallel, the ullage spring can be neglected. Transforming the mass additions to structural modal coordinates yields:

$$\begin{bmatrix} M_L A_R^2 \phi_{XT}^T & \phi_{XT} & \phi_{XT} \\ -M_L A_R \phi_{XT}^T & \phi_{XL} & \phi_{XL} \\ -M_L A_R \phi_{XL}^T & \phi_{XT} & \phi_{XT} \\ \hline M_L A_R \phi_{XL} & & \\ -M_L A_R^2 \phi_{XT} & & \end{bmatrix} \begin{Bmatrix} M_L A_R \phi_{XL}^T \\ -M_L A_R^2 \phi_{XT}^T \\ n_S \\ q_{FT} \end{Bmatrix} = \begin{Bmatrix} 0 \\ - \\ Q_{FT} \end{Bmatrix}$$

or

$$\begin{bmatrix} \frac{M_{LSS}}{M_{LFS}} & \frac{M_{LSF}}{M_{LFF}} \\ \end{bmatrix} \begin{Bmatrix} \ddot{\eta}_S \\ q_{FT} \end{Bmatrix} = \begin{Bmatrix} 0 \\ Q_{FT} \end{Bmatrix} \quad (6)$$

The equations of motion are augmented as indicated in equation (2) for aerodynamics, equation (3) for slosh, and equation (6) for relative flow. After incorporating these enhancements to the structural model, the equations of motion have the form: (double dashes indicate the compression of η_S in the first term)

$$\begin{bmatrix} I + M_{LSS} & \sqrt{M_{SL}} \phi^T ZT & M_{LSF} \\ \hline \hline \sqrt{M_{SL}} \phi ZT & 1 & 0 \\ \hline \hline M_{LFS} & 0 & M_{LFF} \end{bmatrix} \begin{Bmatrix} \ddot{\eta}_S \\ q_{SL} \\ q_{FT} \end{Bmatrix}$$

$$+ \begin{bmatrix} 0 & 0 & | & 0 & | & 0 & || & 0 & | & 0 \\ \hline \hline 0 & 0 & | & 0 & | & 0 & || & 0 & | & 0 \\ \hline \hline 0 & 0 & | & 2\zeta_A \omega_A & | & 0 & || & 0 & | & 0 \\ \hline \hline 0 & 0 & | & 0 & | & 2\zeta_S \omega_S & || & 0 & | & 0 \\ \hline \hline 0 & 0 & | & 0 & | & 0 & || & 2\zeta_{SL} \omega_{SL} & | & 0 \\ \hline \hline 0 & 0 & | & 0 & | & 0 & || & 0 & | & 0 \end{bmatrix} \begin{Bmatrix} \dot{\eta}_{S,1} \\ \dot{\eta}_{S,2} \\ \dot{\eta}_{S,3} \\ \dot{\eta}_S' \\ q_{SL} \\ q_{FT} \end{Bmatrix}$$

$$+ \begin{bmatrix} 0 & 0 & | & 0 & | & 0 & || & 0 & | & 0 \\ \hline \hline 0 & 0 & | & K_A & | & 0 & || & 0 & | & 0 \\ \hline \hline 0 & 0 & | & \omega_A^2 & | & 0 & || & 0 & | & 0 \\ \hline \hline 0 & 0 & | & 0 & | & \omega_S^2 & || & 0 & | & 0 \\ \hline \hline 0 & 0 & | & 0 & | & 0 & || & \omega_{SL}^2 & | & 0 \\ \hline \hline 0 & 0 & | & 0 & | & 0 & || & 0 & | & 0 \end{bmatrix} \begin{Bmatrix} \dot{\eta}_{S,1} \\ \dot{\eta}_{S,2} \\ \dot{\eta}_{S,3} \\ \dot{\eta}_S' \\ q_{SL} \\ q_{FT} \end{Bmatrix} = \begin{Bmatrix} H_{S,1} \\ H_{S,2} \\ H_{S,3} \\ H_S' \\ 0 \\ Q_{FT} \end{Bmatrix} \quad (7)$$

where the H 's are the structural modal forces, I is an identity matrix, and η_S , ω_S , ζ_S are the flexible modal amplitudes, frequencies, and dampings. Defining q_S as the vector η_S , q_{SL} , the equation (7) may be summarized as:

$$\begin{bmatrix} M_{SS} & M_{ST} \\ M_{TS} & M_{TT} \end{bmatrix} \begin{Bmatrix} \ddot{q}_S \\ q_{FT} \end{Bmatrix} + \begin{bmatrix} D_{SS} & 0 \\ 0 & 0 \end{bmatrix} \begin{Bmatrix} \dot{q}_S \\ q_{FT} \end{Bmatrix} + \begin{bmatrix} K_{SS} & 0 \\ 0 & 0 \end{bmatrix} \begin{Bmatrix} q_S \\ q_{FT} \end{Bmatrix} = \begin{Bmatrix} Q_S \\ Q_{FT} \end{Bmatrix} \quad (8)$$

Feedline

Feedline dynamics are of primary importance to the pogo system. The feedline design (fig. 4) was idealized as illustrated in fig. 5. Because of potential interaction of the lateral runs with the structure, primary consideration was given to maintaining the effective lateral run mass and the total system mass. Only one of the two LOX lines was modeled due to symmetry.

A detailed fluid dynamic model was developed of the feedline segments. The feedline model reflects the inertial and compliant characteristics of the fluid and the radial compliance of the line. The model does not include the inertial or compliant properties of the line itself, which are negligible compared with the structure to which it is attached. A compatibility relationship is used to couple the segments. The equations are transformed to relative modal coordinates. An asymmetric equation form is adopted because it facilitates coupling and provides pressures as explicit state variables. The form of the last coordinate is changed to engine weight flow to facilitate coupling to the engine.

The feedline was modeled as 17 segments, each of which was modeled as a discrete mass and spring system. The fluid mass in each segment was divided equally among uniformly spaced discrete masses; the discrete spring rate, which includes the line circumferential elasticity was $= (N - 1) E t \beta A_F / L (d \beta + E t)$ where N is the number of discrete masses, L is the segment length, β is the liquid bulk modulus, and E , t , d , A_F are the pipe's Young's modulus, thickness, diameter, and area. Modeling data for the feedline segments identified in fig. 5 are presented in table 2.

Every segment has a mass at each end. To couple the feedline segments, a compatibility relationship is written at each joint stating the flow into the joint equals the flow out. The last mass of the upstream segment is then eliminated using the compatibility relationship. As an example of a joint with more than two segments, the relationship for C-D-P-Q is:

$$A_{F,C} (q_{F,C58} - q_{R3}) = A_{F,D} (q_{F,D1} - q_{R3}) \\ + A_{F,P} (q_{F,P1} - q_{R3}) + A_{F,Q} (q_{F,Q1} - q_{R3})$$

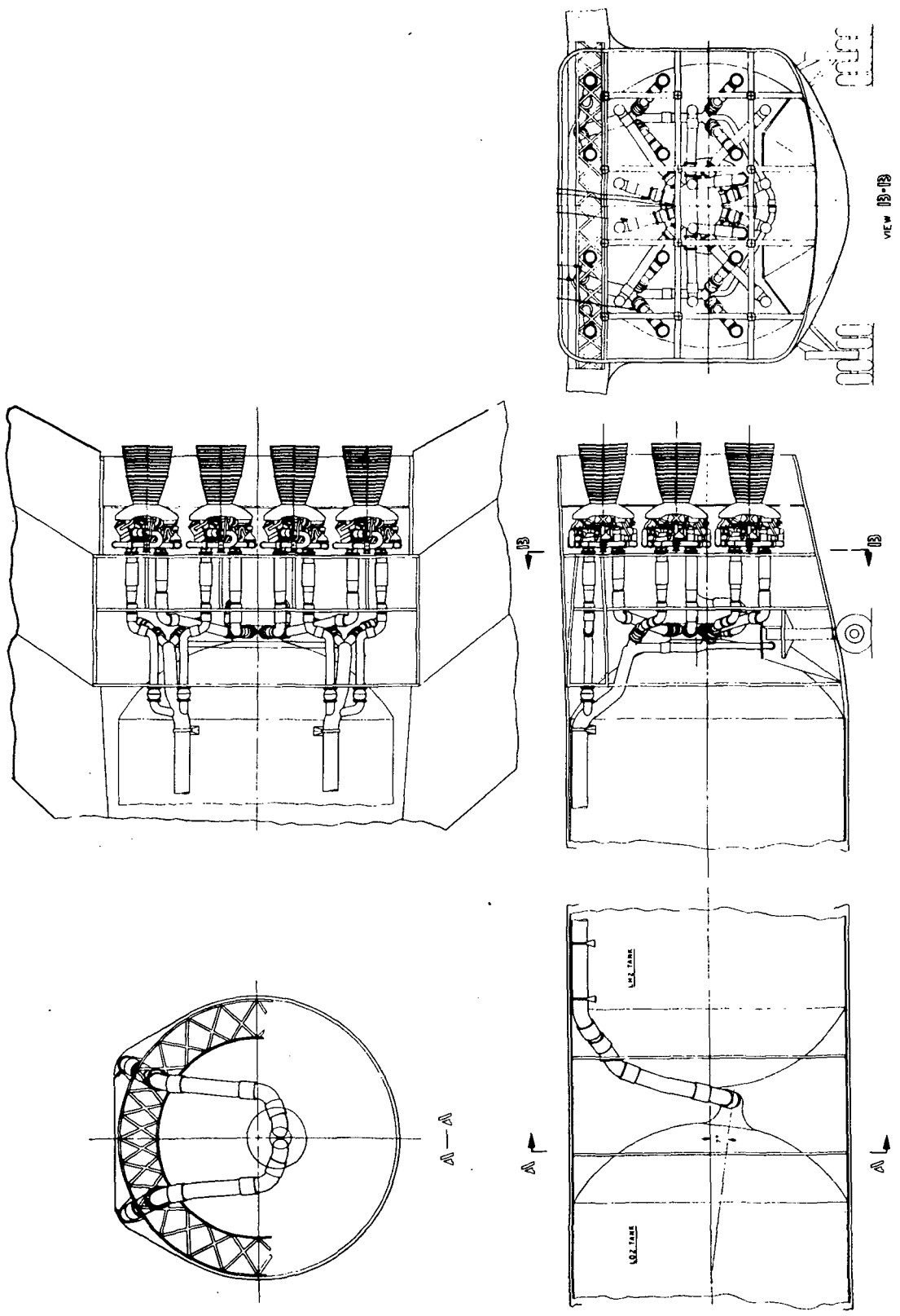


Figure 4. Space Shuttle Feedline Design

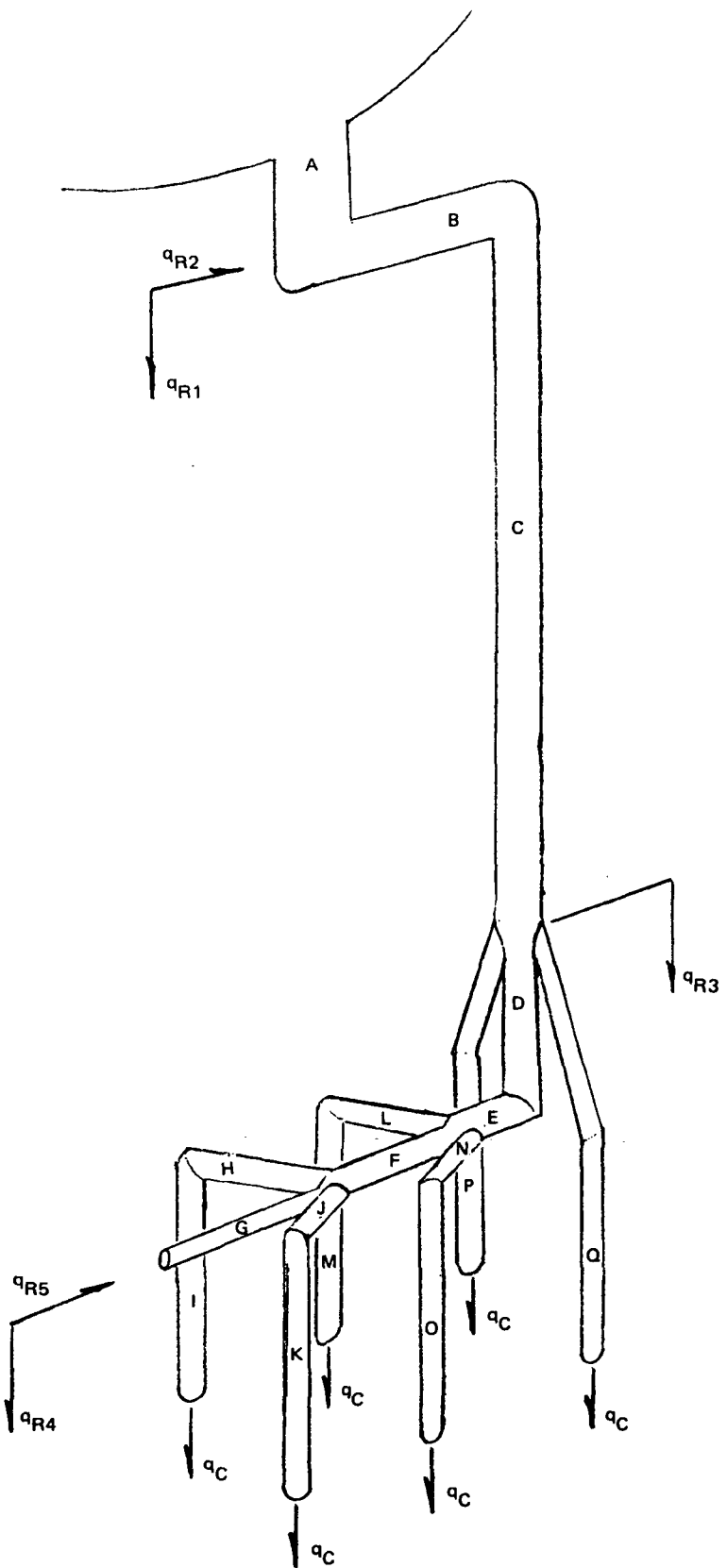


Figure 5. Space Shuttle Feedline Idealization

TABLE 2. SPACE SHUTTLE LOX FEEDLINE MODELING DATA

Segment	Discrete Masses	Length m (in)	Pipe Wall Thickness mm (in)	Pipe Diameter m (in)	Pipe Area m ² (in ²)
A	4	1. 1684 (46.)	6. 3500 (0. 250)	1. 0668 (42.)	0. 893837 (1385. 45)
B	9	5. 3340 (210.)	1. 6510 (0. 065)	0. 5588 (22.)	0. 245245 (380. 13)
C	58	38. 1762 (1503.)	1. 6510 (0. 065)	0. 5588 (22.)	0. 245245 (380. 13)
D	4	2. 5400 (100.)	1. 7780 (0. 070)	0. 4572 (18.)	0. 164174 (254. 47)
E	5	1. 7780 (70.)	1. 7780 (0. 070)	0. 4572 (18.)	0. 164174 (254. 47)
F	5	2. 5400 (100.)	1. 0922 (0. 043)	0. 3302 (13.)	0. 085632 (132. 73)
G	5	4. 3180 (170.)	0. 8128 (0. 032)	0. 2032 (8.)	0. 032432 (50. 27)
H, J, L, N	3	1. 0160 (40.)	1. 0160 (0. 040)	0. 3048 (12.)	0. 072968 (113. 10)
I, K, M, O	6	3. 5560 (140.)	1. 0160 (0. 040)	0. 3048 (12.)	0. 072968 (113. 10)
P, Q	14	6. 7310 (265.)	1. 0160 (0. 040)	0. 3048 (12.)	0. 072968 (113. 10)

LOX Density 1137. 3 kg/m³ (71. 00 lb/ft³)LOX Bulk Modulus 8. 62 x 10⁷ N/m² (1. 25 x 10⁵ lb/in²)Pipe Young's Modulus 1. 79 x 10¹⁰ N/m² (2. 6 x 10⁷ lb/in²)

or

$$q_{F,C58} = \frac{A_{F,D}}{A_{F,C}} q_{F,D1} + \frac{A_{F,P}}{A_{F,C}} q_{F,P1} + \frac{A_{F,Q}}{A_{F,C}} q_{F,Q1} + \left(1 - \frac{A_{F,D} + A_{F,P} + A_{F,Q}}{A_{F,C}} \right) q_{R3} \quad (9)$$

where $A_{F,i}$ is the area of segment i , $q_{F,ij}$ is the displacement of the j th discrete mass in segment i , and q_{Ri} are the displacements of the feedline pipe due to structural motion at reaction coordinate i . There are five reaction coordinates: axial and lateral at the tank bottom, axial at the intersection of segments C, D, P, and Q, and axial and lateral at the lateral manifold, E-F-G. Deflections due to structural rotations were considered small in comparison to lineal deflections and were ignored. The feedline motions at the six engines were assumed to behave identically. This follows from symmetry for pairs I-K, M-O, and P-Q, and is consistent with the small rotation assumption for the remaining groupings, I-K versus M-O, M-O versus P-Q, and I-K versus P-Q. That is, the torque due to thrust differential was neglected.

To verify the assumption of no thrust differential torque, the feedline mode involving fluid motion between I-K and P-Q was isolated and coupled to the closest structural mode. The structural frequency was shifted to maximize the coupling. Both analytical and numerical solutions revealed a highly stable system, verifying the assumption. If the accumulator compliance is eliminated, the feedline mode is raised beyond the frequency range of interest. With these assumptions, the bottom masses of segments I, K, M, O, P, and Q are coupled through six identical springs representing accumulator and cavitation compliance to a single coordinate, q_C , representing the average inertial displacement of fluid into the engines.

The mass and stiffness matrix for the feedline segments were assembled as five reaction coordinates q_{R1} through q_{R5} , the engine fluid displacement q_C , and 154 discrete coordinates, $q_{F,A1}$ through $q_{F,Q14}$. A similarity transformation with a matrix based on the eleven joint compatibility equations was used to couple the segments and reduce the system to q_{R1} through q_{R5} , q_C , and the 143 independent discrete feedline coordinates. The accumulator-cavitation springs were added to the stiffness matrix at this point. Terms in the first six rows and columns of the mass matrix were neglected. This is

equivalent to modifying the segment model such that the last mass in a segment is zero, and augmenting the first mass in the next segment. After these operations, the feedline equations had the form:

$$\begin{bmatrix} 0 & 0 & 0 \\ 0 & 0 & 0 \\ 0 & 0 & M_{FF} \end{bmatrix} \begin{Bmatrix} q_R \\ q_C \\ q_F \end{Bmatrix} + \begin{bmatrix} K_{RR} & K_{RC} & K_{RF} \\ K_{CR} & K_{CC} & K_{CF} \\ K_{FR} & K_{FC} & K_{FF} \end{bmatrix} \begin{Bmatrix} q_R \\ q_C \\ q_F \end{Bmatrix} = \begin{Bmatrix} Q_R \\ Q_C \\ Q_F \end{Bmatrix} \quad (10)$$

The normal modes of the cantilevered system, $q_{R1} = \dots = q_{R5} = q_C = 0$, were calculated. Equation (10) was transformed to relative modal coordinates, and the modal equations were premultiplied by the feedline mode shapes transposed, ϕ_F^T [see equation (11)].

Letting

$$q_F = \phi_F \eta_F - K_{FF}^{-1} K_{FRC} q_{RC}$$

where

$$\begin{bmatrix} K_{FRC} \end{bmatrix} = \begin{bmatrix} K_{FR} & K_{FC} \end{bmatrix} \text{ and } \begin{Bmatrix} q_{RC} \end{Bmatrix} = \begin{Bmatrix} q_R \\ q_C \end{Bmatrix}$$

yields

$$\begin{bmatrix} 0 & 0 \\ -\phi_F^T M_{FF} K_{FF}^{-1} K_{FRC} & I \end{bmatrix} \begin{Bmatrix} q_{RC} \\ \eta_F \end{Bmatrix} + \begin{bmatrix} 0 & 0 \\ 0 & 2 \zeta_F \omega_F \end{bmatrix} \begin{Bmatrix} q_{RC} \\ \eta_F \end{Bmatrix} + \begin{bmatrix} K_{RCRC} & K_{RCF} K_{FF}^{-1} K_{FRC} \\ 0 & \frac{K_{RCF} \phi_F}{\omega_F^2} \end{bmatrix} \begin{Bmatrix} q_{RC} \\ \eta_F \end{Bmatrix} = \begin{Bmatrix} Q_{RC} \\ H_F \end{Bmatrix} \quad (11)$$

where ω_F , η_F , H_F are the feedline natural frequencies, modal amplitudes, and generalized forces and where modal damping, $\zeta_F = 0.01$, was introduced in the equations. It may be noted that $K_{RCRC} - K_{RCF} K_{FF}^{-1} K_{FRC}$, the reduced reaction stiffness, is zero since the fluid is free to move in response to a reaction displacement. This unsymmetric formulation retains the reaction forces explicitly.

The weight flow through the engine, W , is determined from the inertial displacement as $\rho g A_E (\dot{q}_C - \dot{X}_E)$ where ρ is the density, g is the acceleration of gravity, A_E is the feedline area at the engine, and X_E is the engine axial displacement. With this substitution the coordinate transformation and the feedline equations of motion of equation (11) assume the form:

$$\begin{Bmatrix} q_F \\ \end{Bmatrix} = \begin{bmatrix} -K_{FF}^{-1} K_{FRC} & | & \phi_F & | & -\frac{1}{\rho g A_E} & K_{FF}^{-1} K_{FC} \\ | & | & | & | & | & | \\ \end{bmatrix} \begin{Bmatrix} \dot{q}_{RE} \\ \eta_F \\ W \end{Bmatrix}$$

where

$$\begin{Bmatrix} q_{RE} \\ \dot{X}_E \end{Bmatrix} = \begin{Bmatrix} q_R \\ \dot{X}_E \end{Bmatrix}$$

and

$$\begin{bmatrix} 0 & | & 0 & | & 0 \\ | & I & | & | & | \\ -\phi_F^T M_{FF} & K_{FF}^{-1} K_{FRC} & | & -\frac{1}{\rho g A_E} & \phi_F^T M_{FF} & K_{FF}^{-1} K_{FC} \\ | & | & | & | & | & | \\ \end{bmatrix} \begin{Bmatrix} \ddot{q}_{RE} \\ \ddot{\eta}_F \\ \ddot{W} \end{Bmatrix}$$

$$+ \begin{bmatrix} 0 & | & 0 & | & 0 \\ | & 2 & | & \zeta_F & | & \omega_F & | & 0 \\ 0 & | & 0 & | & 0 \end{bmatrix} \begin{Bmatrix} \dot{q}_{RE} \\ \eta_F \\ W \end{Bmatrix} + \begin{bmatrix} 0 & | & K_{RCF} \phi_F & | & 0 \\ | & \omega_F^2 & | & | & | \\ 0 & | & 0 & | & 0 \end{bmatrix} \begin{Bmatrix} \dot{q}_{RE} \\ \eta_F \\ W \end{Bmatrix} = \begin{Bmatrix} Q_{RC} \\ H_F \\ \end{Bmatrix} \quad (12)$$

Control

The Space Shuttle pitch plane thrust vector control system was used in this study. A block diagram of this control system is shown in fig. 6. The commanded and actual engine gimbal deflection are assumed identical since actuator resonances are above the frequency range of interest. However inertial effects of the gimballed engine, sometimes referred to as "tail wags dog", were within the range of interest. The "tail wags dog" equations are developed and incorporated in a matrix format with the control equations from the block diagram.

The mass matrix contributions of the engine were removed from the gimbal plane structural coordinates, Z_G , and θ_G and assigned to the center of mass (c.m.) engine coordinates, Z_E and θ_E . The additions to the structural equations have the form:

$$\begin{bmatrix} -M_E & M_E \lambda & 0 & 0 \\ M_E \lambda & -\left(I_E + M_E \lambda^2\right) & 0 & 0 \\ 0 & 0 & M_E & 0 \\ 0 & 0 & 0 & I_E \end{bmatrix} \begin{Bmatrix} \ddot{Z}_G \\ \ddot{\theta}_G \\ Z_E \\ \theta_E \end{Bmatrix} = \begin{Bmatrix} -F_A + F_C \\ -M_A + F_A \lambda \\ F_A \\ M_A \end{Bmatrix} \quad (13)$$

where M_E and I_E are the engine mass and inertia, F_C is the control force, F_A and M_A are the actuator force and moment, and λ is the distance from c.m. to gimbal plane. The engine coordinates are related to the commanded gimbal angle, δ , by: $\theta_E = \theta_G + \delta$, and $Z_E = Z_G - \lambda(\theta_G + \delta)$. Equation (13) is transformed to relative coordinates:

$$\begin{bmatrix} 0 & 0 & -M_E \lambda & \\ 0 & 0 & I_E + M_E \lambda^2 & \\ -M_E \lambda & I_E + M_E \lambda^2 & I_E + M_E \lambda^2 & \end{bmatrix} \begin{Bmatrix} \ddot{Z}_G \\ \ddot{\theta}_G \\ \delta \end{Bmatrix} = \begin{Bmatrix} T \delta \\ 0 \\ F_\delta \end{Bmatrix} \quad (14)$$

or

$$\begin{Bmatrix} F_{ZG} \\ F_{\theta G} \end{Bmatrix} = \begin{Bmatrix} T \\ 0 \end{Bmatrix} \delta + \begin{Bmatrix} M_E \lambda \\ -\left(I_E + M_E \lambda^2\right) \end{Bmatrix} \ddot{\delta}$$

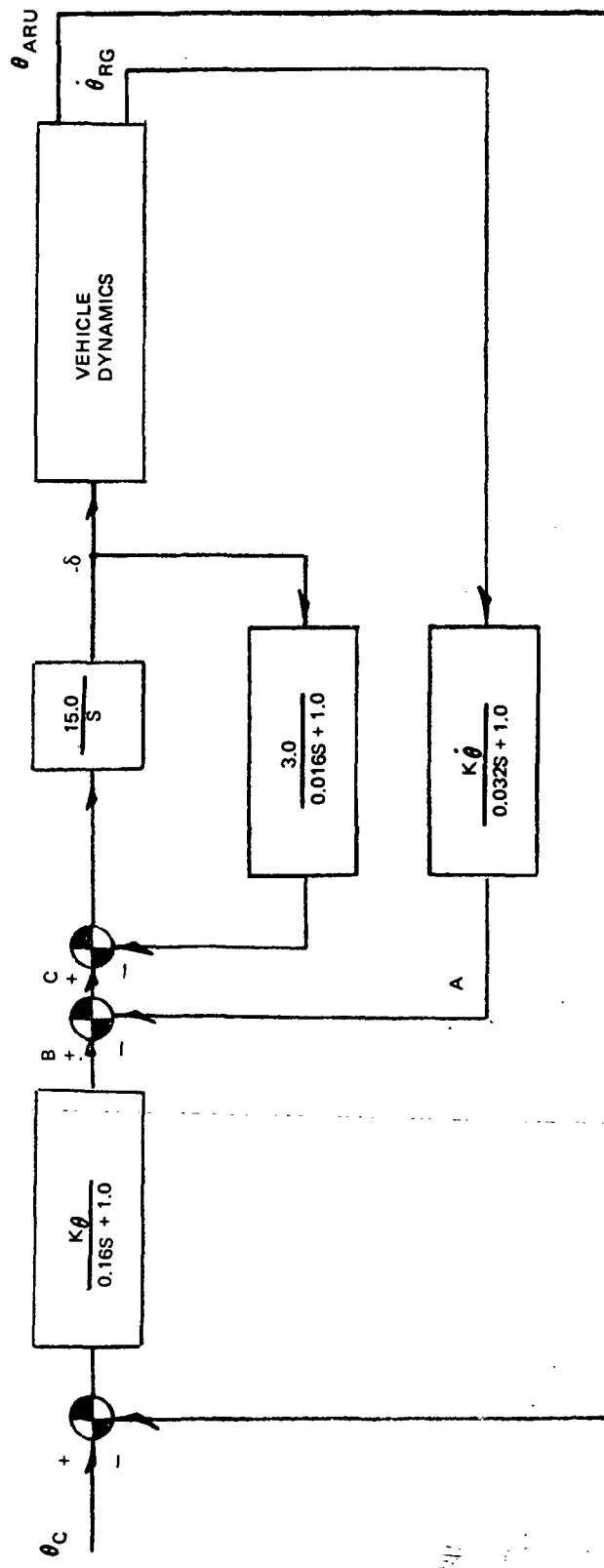


Figure 6. Block Diagram of Pitch Control System

where F_{ZG} and $F_{\theta G}$ are the net lateral force and moment on the gimbal, T is the total thrust, $12 \times 2.45 \times 10^6$ Newtons ($12 \times 550,000$ lb), and where it has been noted that internal actuator forces cancel and that the lateral control force is approximated by the thrust times the angle (in radians) for small gimbal angles. The dynamic equation in δ is dropped since the actual angle is assumed equal to the commanded angle. The quantities $M_E \lambda$ and $I_E + M_E \lambda^2$ were computed indirectly from the tail wags dog frequencies, which are defined as the frequency at which the modal force is zero.

If the gimbal feedback loop is reduced, the control system may be expressed as a matrix polynomial in the Laplace operator, s , and the dummy control variables, A , B , C , identified in fig. 6.

$$-\delta = \frac{15}{s} \left(C + \frac{3\delta}{1 + .016s} \right)$$

gives

$$(15 + .24s)(B - A) + (.016s^2 + s + 45)\delta = 0$$

so,

$$\begin{bmatrix} 1. & 0 & | & (I_E + M_E \lambda^2)s^2 & 0 & | & 0 & | & 0 & | & 0 \\ 0 & 1. & | & -M_E \lambda s^2 - T & 0 & | & 0 & | & 0 & | & 0 \\ 0 & 0 & | & -.016s^2 & 15. & | & -15. & | & 0 & | & 0 \\ 0 & 0 & | & -s - 45. & +24s & | & -.24s & | & 0 & | & 0 \\ 0 & 0 & | & 0 & 0.032s & | & 0 & | & -K_\theta s & | & 0 \\ 0 & 0 & | & 0 & +1 & | & 0 & | & 0 & | & 0 \\ 0 & 0 & | & 0 & 0 & | & .16s & | & 0 & | & K_\theta \end{bmatrix} \begin{Bmatrix} F_{\theta G} \\ F_{ZG} \\ \delta \\ A \\ B \\ \theta_{RG} \\ \theta_{ARU} \end{Bmatrix} = 0 \quad (15)$$

where θ_{RG} , θ_{ARU} are the pitch rotation measured at the rate gyro and the attitude reference unit.

Engine

Engine dynamics are of primary importance to the pogo system. Space Shuttle main engine dynamic characteristics were obtained from North American Rockwell Corporation, Rocketdyne Division. This engine model was of a preliminary nature and neglected cavitation effects, generally important in pump dynamic gains. Measurements on existing engines and other candidate shuttle engine models show substantially greater gains. For these reasons the engine model was a primary candidate for parametric variation. As provided, the transfer function from LOX suction pressure, P_S , to chamber pressure, P_C and LOX weight flow, \dot{W} , are:

$$\frac{P_C}{P_S} = \frac{0.25s \left(1 + \frac{s}{4.6\pi} \right)}{\left(1 + \frac{s}{\pi} \right)^2},$$

and

$$\frac{\dot{W}}{P_S} = \mu \frac{0.075s \left(1 + \frac{s}{4.6\pi} \right)}{\left(1 + \frac{s}{\pi} \right)^2} \quad (16)$$

where

$$\mu = 6.4516 \times 10^{-4} \frac{m^2}{sec} \left(1.0 \frac{in.^2}{sec} \right)$$

The fuel side transfer functions provided by the engine manufacturer were at least two orders of magnitude smaller and were neglected. Thrust, T , is obtained from chamber pressure by multiplying by the effective area, $0.1181m^2$ (183.0 in.^2). The transfer function P_C/P_S is presented as a function of frequency in fig. 7 and fig. 8. It may be noted that a gain of at least 0.618 is required for the thrust oscillation to exceed the pressure times area oscillatory load acting down on the engine. Although the engine never reaches that level, other candidate engines exceed it.

The axial force, F_{XG} , is the sum of the thrust and the product of the suction pressure, P_S , and the line area, $12 \times A_E$, so the equation may be written

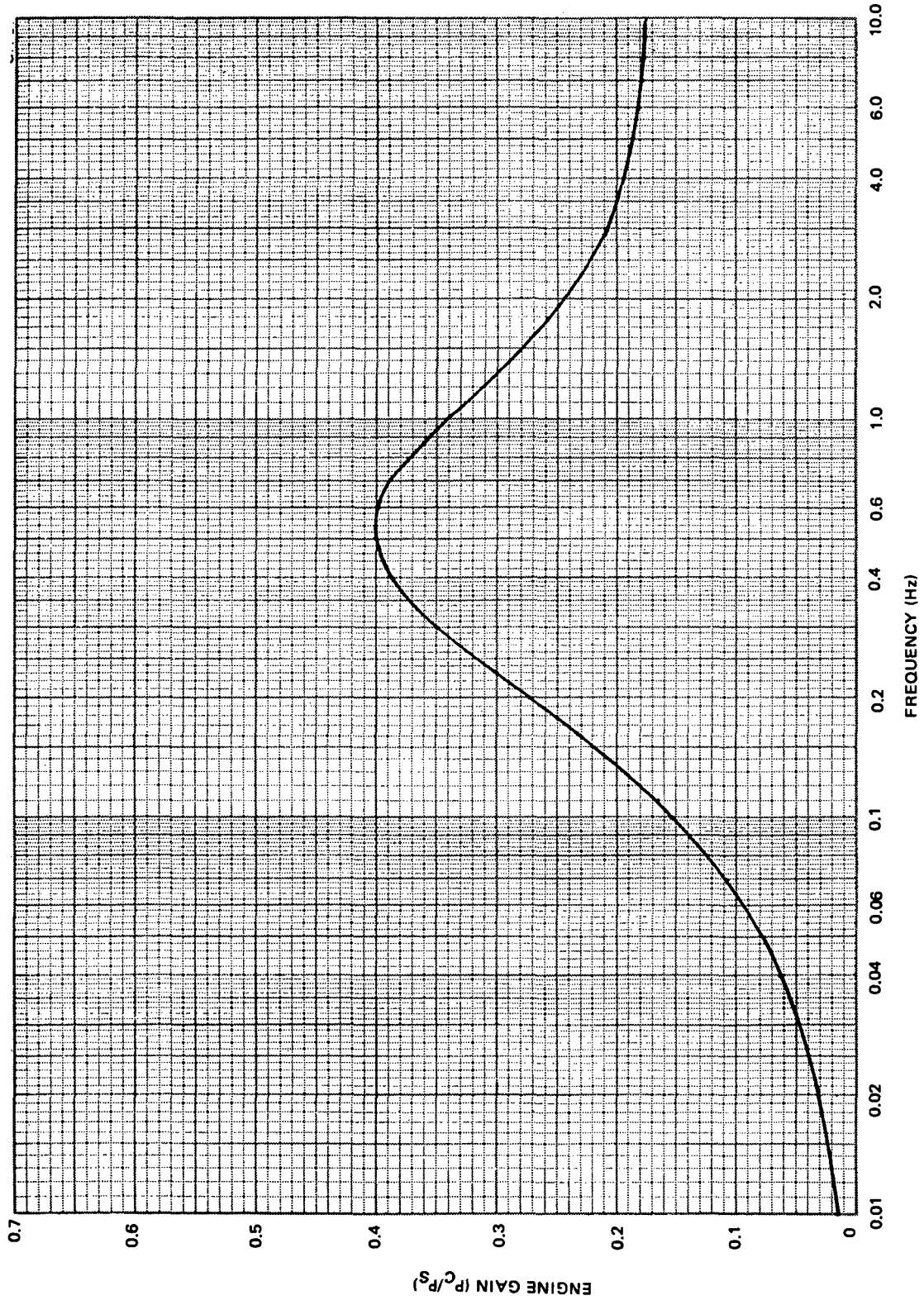


Figure 7. Space Shuttle Main Engine Gain Versus Frequency

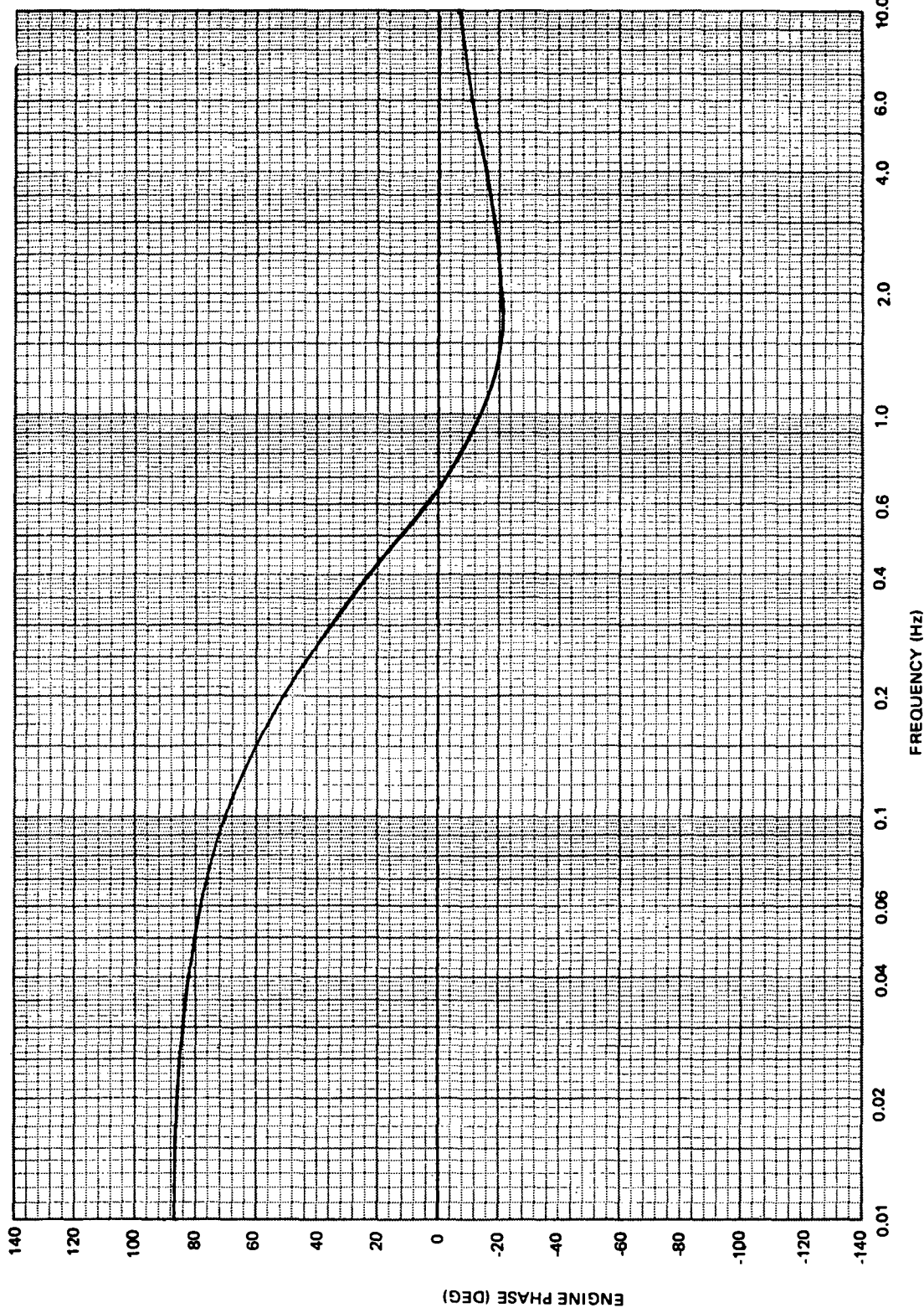


Figure 8. Space Shuttle Main Engine Phase Versus Frequency

$$\begin{bmatrix} -0.075\pi \left(\frac{1}{4.6} s^2 + \pi s \right) & s^2 + 2\pi s + \pi^2 & 0 & 0 \\ -549\pi \left(\frac{1}{4.6} s^2 + \pi s \right) & 0 & s^2 + 2\pi s + \pi^2 & 0 \\ 12 A_E & 0 & -1 & -1 \end{bmatrix} \begin{Bmatrix} P_S \\ W \\ T \\ F_{XG} \end{Bmatrix}$$

or

(17)

$$[M_{EE}] \begin{Bmatrix} P_S \\ W \\ T \\ F_{XG} \end{Bmatrix} + [D_{EE}] \begin{Bmatrix} P_S \\ W \\ T \\ F_{XG} \end{Bmatrix} + [K_{EE}] \begin{Bmatrix} P_S \\ W \\ T \\ F_{XG} \end{Bmatrix} = \{ 0 \}$$

where M_{EE} , D_{EE} , and K_{EE} , the coefficient matrices of the differential equation, denote the s^2 , s , and constant portions of the matrix polynomial equation.

Coupled System

The individual structural, feedline, engine, and control models are combined in one system of equations. To accomplish this, a global state vector was selected, and the feedline and structure are transformed to the state space. The feedline and structure are coupled and the control system is expressed in the global coordinates. Combining the engine, control, and coupled structure-feedline systems gives the final state equations of motion.

The global coordinate system, or state space vector, was formed as follows: structural generalized coordinates, q_S , feedline modes, η_F , LOX tank pressure, P_T , engine suction pressure, P_S , engine weight flow, \dot{W} , total thrust, T , gimbal rotation, δ , control variable A , control variable B . This is a mixed state vector including both displacement and force type elements. The formulation results in some dependent equations which were eliminated automatically by the computer algorithm.

The feedline equations are first transformed to global coordinates. The engine and reaction coordinates are then expressed in terms of the appropriate rows of the composite structural mode shape matrix, ϕ_{SR} , which include

rigid, flexible, and slosh modes. The coordinate transformation and the equations of motion (see equation (12)) assume the form:

if

$$\{q_{RE}\} = [\phi_{SRC}] \{q_S\}$$

then

$$\{q_F\} = \left[-K_{FF}^{-1} K_{FRC} \phi_{SRC} \begin{array}{|c|c|c|} \hline \phi_F & 0 & 0 \\ \hline \end{array} \right] \frac{-1}{\rho g A_E} K_{FF}^{-1} K_{FC} \left\{ \begin{array}{l} q_S \\ \eta_F \\ P_T \\ P_S \\ W \end{array} \right\}$$

(18)

and

$$\left[\begin{array}{ccccc} 0 & 0 & 0 & 0 & 0 \\ -\phi_F^T M_{FF} K_{FF}^{-1} K_{FRC} \phi_{SRC} & I & 0 & 0 & \frac{-1}{\rho g A_E} \phi_F^T M_{FF} K_{FF}^{-1} K_{FC} \\ \hline 0 & 0 & 0 & 0 & 0 \\ -\phi_F^T M_{FF} K_{FF}^{-1} K_{FRC} \phi_{SRC} & I & 0 & 0 & \frac{-1}{\rho g A_E} \phi_F^T M_{FF} K_{FF}^{-1} K_{FC} \\ \hline \end{array} \right] \left\{ \begin{array}{l} q_S \\ \eta_F \\ P_T \\ P_S \\ W \end{array} \right\} + \left[\begin{array}{ccccc} 0 & 0 & 0 & 0 & 0 \\ 0 & 2 \zeta_F \omega_F & 0 & 0 & 0 \\ \hline 0 & 0 & 0 & 0 & 0 \\ 0 & 2 \zeta_F \omega_F & 0 & 0 & 0 \\ \hline \end{array} \right] \left\{ \begin{array}{l} q_S \\ \eta_F \\ P_T \\ P_S \\ W \end{array} \right\} + \left[\begin{array}{ccccc} 0 & K_{RCF} \phi_F & 0 & 0 & 0 \\ 0 & \omega_F^2 & 0 & 0 & 0 \\ \hline 0 & 0 & 0 & 0 & 0 \\ 0 & \omega_F^2 & 0 & 0 & 0 \\ \hline \end{array} \right] \left\{ \begin{array}{l} q_S \\ \eta_F \\ P_T \\ P_S \\ W \end{array} \right\} = \left\{ \begin{array}{l} Q_{RC} \\ H_F \end{array} \right\}$$

The force on the engine fluid displacement, Q_C , is the negative of the suction pressure, $-P_S$, times the area, $6 \times A_E$. The only source of modal force on the feedline, H_F , is the tank pressure, P_T times the area of the feedline at the tank, A_{FT} , times the value of the feedline mode shape at the top of the line. Making these substitutions and transforming to modal structural force yields:

Let

$$H_F = \phi_{F,1}^T A_{FT} P_T$$

then

$$\begin{bmatrix} 0 & 0 & 0 & 0 \\ 0 & 0 & 0 & 0 \\ -\phi_F^T M_{FF} K_{FF}^{-1} K_{FRC} \phi_{SRC} & I & 0 & 0 \\ -\frac{1}{\rho g A_E} \phi_F^T M_{FF} K_{FF}^{-1} K_{FC} \end{bmatrix} \begin{Bmatrix} q_S \\ \eta_F \\ P_T \\ P_S \\ W \end{Bmatrix}$$

$$+ \begin{bmatrix} 0 & 0 & 0 & 0 & 0 \\ 0 & 0 & 0 & 0 & 0 \\ 0 & 2\zeta_F \omega_F & 0 & 0 & 0 \end{bmatrix} \begin{Bmatrix} q_S \\ \eta_F \\ P_T \\ P_S \\ W \end{Bmatrix}$$

$$+ \begin{bmatrix} 0 & \phi_{SR}^T K_{RF} \phi_F & 0 & 0 & 0 \\ 0 & K_{CF} \phi_F & 0 & 6A_E & 0 \\ 0 & \omega_F^2 & -\phi_{F,1}^T A_{FT} & 0 & 0 \end{bmatrix} \begin{Bmatrix} q_S \\ \eta_F \\ P_T \\ P_S \\ W \end{Bmatrix} = \begin{Bmatrix} \phi_{SR}^T Q_R \\ 0 \\ 0 \end{Bmatrix} \quad (19)$$

where ϕ_{SR} is the first five rows of ϕ_{SRC} .

Similarly, the structural equations are converted to global coordinates, using the first row of the coordinate transform in equation (18).

$$\begin{bmatrix} M_{SS} - M_{ST} K_{FF,1}^{-1} K_{FRC} \phi_{SRC} & M_{ST} \phi_{F,1} & 0 & 0 & -\frac{1}{\rho g A_E} M_{ST} K_{FF,1}^{-1} K_{FC} \\ \vdots & \vdots & \vdots & \vdots & \vdots \\ M_{TS} - M_{TT} K_{FF,1}^{-1} K_{FRC} \phi_{SRC} & M_{TT} \phi_{F,1} & 0 & 0 & -\frac{1}{\rho g A_E} M_{TT} K_{FF,1}^{-1} K_{FC} \end{bmatrix} \begin{Bmatrix} q_S \\ \eta_F \\ P_T \\ P_S \\ W \end{Bmatrix}$$

$$+ \begin{bmatrix} D_{SS} & 0 & 0 & 0 & 0 \\ \vdots & \vdots & \vdots & \vdots & \vdots \\ 0 & 0 & 0 & 0 & 0 \end{bmatrix} \begin{Bmatrix} q_S \\ \eta_F \\ P_T \\ P_S \\ W \end{Bmatrix} + \begin{bmatrix} K_{SS} & 0 & 0 & 0 & 0 \\ \vdots & \vdots & \vdots & \vdots & \vdots \\ 0 & 0 & 0 & 0 & 0 \end{bmatrix} \begin{Bmatrix} q_S \\ \eta_F \\ P_T \\ P_S \\ W \end{Bmatrix} = \begin{Bmatrix} Q_S \\ Q_{FT} \end{Bmatrix} \quad (20)$$

The generalized force on the tank fluid, Q_{FT} , is the negative of the pressure, $-P_T$, times the area of the two feedlines, $2 \times A_{FT}$. The generalized force on the structure has two sources, the negative of the reaction forces on the two feedlines, [equation (19)] and the gimbal forces. Combining the feedline equations (19) with the structural equation (20) yields equation (21).

Let

$$Q_S = -2\phi_{SR}^T Q_R + \phi_{SXG}^T F_{XG} + \phi_{S\theta G}^T F_{\theta G} + \phi_{SZG}^T F_{ZG}$$

Then

$$\begin{bmatrix} M_{SS} - M_{ST} K_{FF,1}^{-1} K_{FRC} \phi_{SRC} & M_{ST} \phi_{F,1} & 0 & 0 & -\frac{1}{\rho g A_E} M_{ST} K_{FF,1}^{-1} K_{FC} & 0 & 0 & 0 & 0 \\ M_{TS} - M_{TT} K_{FF,1}^{-1} K_{FRC} \phi_{SRC} & M_{TT} \phi_{F,1} & 0 & 0 & \frac{1}{\rho g A_E} M_{TT} K_{FF,1}^{-1} K_{FC} & 0 & 0 & 0 & 0 \\ -\phi_F^T M_{FF} K_{FF}^{-1} K_{FRC} \phi_{SRC} & I & 0 & 0 & \frac{1}{\rho g A_E} \phi_F^T M_{FF} K_{FF}^{-1} K_{FC} & 0 & 0 & 0 & 0 \\ 0 & 0 & 0 & 0 & 0 & 0 & 0 & 0 & 0 \end{bmatrix} \begin{Bmatrix} q_S \\ \eta_F \\ p_T \\ p_S \\ w \\ t \\ F_{XG} \\ F_{\theta G} \\ F_{ZG} \end{Bmatrix}$$

$$+ \begin{bmatrix} D_{SS} & 0 & 0 & 0 & 0 & 0 & 0 & 0 & 0 \\ 0 & 0 & 0 & 0 & 0 & 0 & 0 & 0 & 0 \\ 0 & 2 \zeta_F \omega_F & 0 & 0 & 0 & 0 & 0 & 0 & 0 \\ 0 & 0 & 0 & 0 & 0 & 0 & 0 & 0 & 0 \end{bmatrix} \begin{Bmatrix} q_S \\ \eta_F \\ p_T \\ p_S \\ w \\ t \\ F_{XG} \\ F_{\theta G} \\ F_{ZG} \end{Bmatrix} \quad (21)$$

$$+ \begin{bmatrix} K_{SS} 2 \phi_{SR}^T K_{RF} \phi_F & 0 & 0 & 0 & -\phi_{SXG}^T & -\phi_{S\theta G}^T & -\phi_{SZG}^T \\ 0 & 0 & 2 A_{FT} & 0 & 0 & 0 & 0 \\ 0 & \omega_F^2 & -\phi_{F,1}^T A_{FT} & 0 & 0 & 0 & 0 \\ 0 & K_{CF} \phi_F & 0 & 6 A_E & 0 & 0 & 0 \end{bmatrix} \begin{Bmatrix} q_S \\ \eta_F \\ p_T \\ p_S \\ w \\ t \\ F_{XG} \\ F_{\theta G} \\ F_{ZG} \end{Bmatrix} = \begin{Bmatrix} 0 \\ \dots \\ 0 \\ 0 \\ \dots \\ 0 \\ \dots \\ 0 \end{Bmatrix}$$

where ϕ_{SXG} , $\phi_{S\theta G}$, ϕ_{SZG} are the axial, rotational, and lateral structural mode shapes at the gimbal.

Since the coefficients of \dot{W} and W are zero, the system can be transformed from a state vector involving W to one involving \dot{W} by moving the associated column of the mass matrix to the damping matrix. If this is done and the resulting matrices are denoted M_S , D_S , K_S , the equations may be written:

$$\begin{bmatrix} M_S \\ \vdots \\ q_S \\ \eta_F \\ P_T \\ P_S \\ \dot{W} \\ T \\ F_{XG} \\ F_{\theta G} \\ F_{ZG} \end{bmatrix} + \begin{bmatrix} D_S \\ \vdots \\ q_S \\ \eta_F \\ P_T \\ P_S \\ \dot{W} \\ T \\ F_{XG} \\ F_{\theta G} \\ F_{ZG} \end{bmatrix} + \begin{bmatrix} K_S \\ \vdots \\ q_S \\ \eta_F \\ P_T \\ P_S \\ \dot{W} \\ T \\ F_{XG} \\ F_{\theta G} \\ F_{ZG} \end{bmatrix} = \{0\} \quad (22)$$

The control system, equation (15), is expressed in global coordinates by noting that the rotation at the rate gyro and the attitude reference unit can be expressed in terms of the associated rows of the structural mode shape matrix, ϕ_{SRG} and ϕ_{SARU} , as

$$\left\{ \frac{\theta_{RG}}{\theta_{ARU}} \right\} = \left[\frac{\phi_{SRG}}{\phi_{SARU}} \right] \{q_S\}$$

So

$$\left[\begin{array}{cccccc|c|c|c} 0 & 0 & 0 & 0 & 0 & 0 & 1. & 0 & s^2(I_E + M_E \lambda^2) & 0 & 0 \\ 0 & 0 & 0 & 0 & 0 & 0 & 1. & -s^2 M_E \lambda - T & 0 & 0 \\ 0 & 0 & 0 & 0 & 0 & 0 & 0 & -.016 s^2 - s - 45. & .24s + 15. & -.24s - 15. \\ -s K_\theta \Phi_{SRG} & 0 & 0 & 0 & 0 & 0 & 0 & 0 & .032s + 1. & 0 \\ K_\theta \Phi_{SARU} & 0 & 0 & 0 & 0 & 0 & 0 & 0 & 0 & .16s + 1. \end{array} \right] = \left\{ \begin{array}{l} q_S \\ n_F \\ P_T \\ P_S \\ \dot{W} \\ T \\ F_{XG} \\ F_{\theta G} \\ F_{ZG} \\ \delta \\ A \\ B \end{array} \right\} = \left\{ \begin{array}{l} 0 \\ 0 \\ 0 \\ 0 \\ 0 \\ 0 \\ 0 \\ 0 \\ 0 \\ 0 \\ 0 \\ 0 \end{array} \right\}$$

or

$$[M_C] \{ \ddot{x} \} + [D_C] \{ \dot{x} \} + [K_C] \{ x \} = \{ 0 \} \quad (23)$$

where X denotes the state vector and M_C , D_C , K_C the coefficients of the equivalent differential equation, denote the s^2 , s , and constant terms of the matrix polynomial equation.

Combining these control equations (23) with the coupled feedline-structure equations (22) and the engine equations (17) yields:

$$\begin{bmatrix} M_S & & & 0 & 0 & 0 \\ 0 & 0 & 0 & M_{EE} & 0 & 0 \\ & & & & 0 & 0 \\ & & & & & 0 \end{bmatrix} \left\{ \begin{array}{c} \ddot{x} \\ \vdots \end{array} \right\}$$

M_C

$$+ \begin{bmatrix} D_S & & & 0 & 0 & 0 \\ 0 & 0 & 0 & D_{EE} & 0 & 0 \\ & & & & 0 & 0 \\ & & & & & 0 \end{bmatrix} \left\{ \begin{array}{c} \dot{x} \\ \vdots \end{array} \right\}$$

D_C

$$+ \begin{bmatrix} K_S & & & 0 & 0 & 0 \\ 0 & 0 & 0 & K_{EE} & 0 & 0 \\ & & & & 0 & 0 \\ & & & & & 0 \end{bmatrix} \left\{ \begin{array}{c} x \\ \vdots \end{array} \right\} = \begin{bmatrix} 0 \\ \vdots \\ 0 \\ \vdots \\ 0 \end{bmatrix}$$

K_C

or

$$[M] \left\{ \begin{array}{c} \ddot{x} \\ \vdots \end{array} \right\} + [D] \left\{ \begin{array}{c} \dot{x} \\ \vdots \end{array} \right\} + [K] \left\{ \begin{array}{c} x \\ \vdots \end{array} \right\} = \left\{ \begin{array}{c} 0 \\ \vdots \\ 0 \\ \vdots \\ 0 \end{array} \right\} \quad (24)$$

The equations of motion for the two uncoupled systems, pogo alone and control alone, can be accommodated by dropping the rows and columns associated with W and T , or with $F_{\theta G}$, F_{ZG} , δ , A , and B , respectively.

STABILITY INVESTIGATION

The mathematical model developed in the previous section was used to investigate the nature of pogo-control interaction. The model was investigated in four configurations: control system only active, engine system only active, both systems active, and neither system active. This section discusses the method selected for stability investigation and the selection of a

baseline configuration. The sensitivity of the interaction and stability to parametric variations was investigated. The only deviation from a linear relationship between the eigenvalues of the four configurations was observed in the region of very close roots. This interaction was further investigated through multiple parametric variations. The following symbols have been used to identify the curves in the figures: A, aero mode (the rigid-body pitch mode), S_i , ith structural mode (the first three of which are rigid body), and F_i , the ith feedline mode.

Method

The system stability was evaluated on the basis of closed-loop roots. The type of linear relationship expected is discussed, and an interaction coefficient is defined to evaluate the deviation from linearity, which will be referred to as interaction.

Stability characteristics were evaluated on the basis of the fraction of critical damping associated with the system eigenvalues. The eigenvalues were determined by assuming an exponential solution, $X = \bar{X} e^{st}$, to the homogeneous system equations. The roots of the characteristic equation, determinant $(s^2 M + sD + K) = 0$, provide the eigenvalues, s_i ; the non-trivial solutions of $(s_i^2 M + s_i D + K) \bar{X}_i = 0$ provide the associated eigenvectors, \bar{X}_i . If a_i and b_i are the real and complex parts of the i th eigenvalue, s_i , the undamped natural frequency, ω_i , and the fraction of critical damping, ζ_i , are defined by

$$\omega_i = \sqrt{a_i^2 + b_i^2}$$

and

$$\zeta_i = -a_i / \omega_i \quad (25)$$

A negative fraction of critical damping indicates an unstable system; positive values indicate stability.

The eigenvalues of the structural system are dominated by the imaginary part for a lightly damped structure. A small perturbation to the system equations will produce a small variation in the eigenvalues. The change in frequency is small. However, since the real part of the eigenvalue is already small, the change in damping may be relatively large. If two small perturbations are made to the system equations, the variation in the eigenvalues may be approximated by the sum of the two perturbations applied independently. This corresponds to retaining only the linear terms in a power series expansion of the characteristic equation. Since the frequency is nearly constant, the variation in damping is also approximated by the sum of the variations associated with applying the perturbations independently. In particular, if the fractions of critical damping in any particular mode are: ζ_O for the structural model alone, ζ_P for the structure with the

engine system, ζ_C for the structure with control system, and ζ_{PC} for the combined system, the following relationship should be approximately true:

$$\zeta_{PC} \approx \zeta_O + (\zeta_P - \zeta_O) + (\zeta_C - \zeta_O)$$

or (26)

$$\zeta_{PC} \approx \zeta_P + \zeta_C - \zeta_O$$

To provide a measure of the accuracy of this approximation, an interaction coefficient, IC , is defined for each mode as:

$$IC \zeta_O = (\zeta_P + \zeta_C - \zeta_O) - \zeta_{PC} \quad (27)$$

$$IC = \frac{\zeta_P + \zeta_C - \zeta_{PC}}{\zeta_O} - 1$$

A positive interaction coefficient indicates a less stable combined system than would be expected by the linear combination hypothesis; a negative coefficient, a more stable combined system. For those modes in which the interaction coefficient is small compared to one, the linear combination hypothesis is supported.

Baseline

To improve the computational efficiency, or to make the system more relevant to the interaction problem, a baseline configuration was selected about which subsequent parametric variations would be made. The slosh mode was eliminated, the accumulators were removed, the number of modes retained was reduced, and the 25 percent burn time was selected.

The eigenvalues of the coupled system as developed in the analytical model had a marginally unstable slosh mode with respect to the control system. The source of the instability was traced to locating the slosh degree of freedom too far aft. To evaluate the importance of slosh, the system eigenvalues were recomputed without slosh. A comparison of the eigenvalues with and without slosh showed no significant effect. The 25 percent burn time comparison is presented in fig. 9. The slosh mode was therefore deleted from subsequent runs.

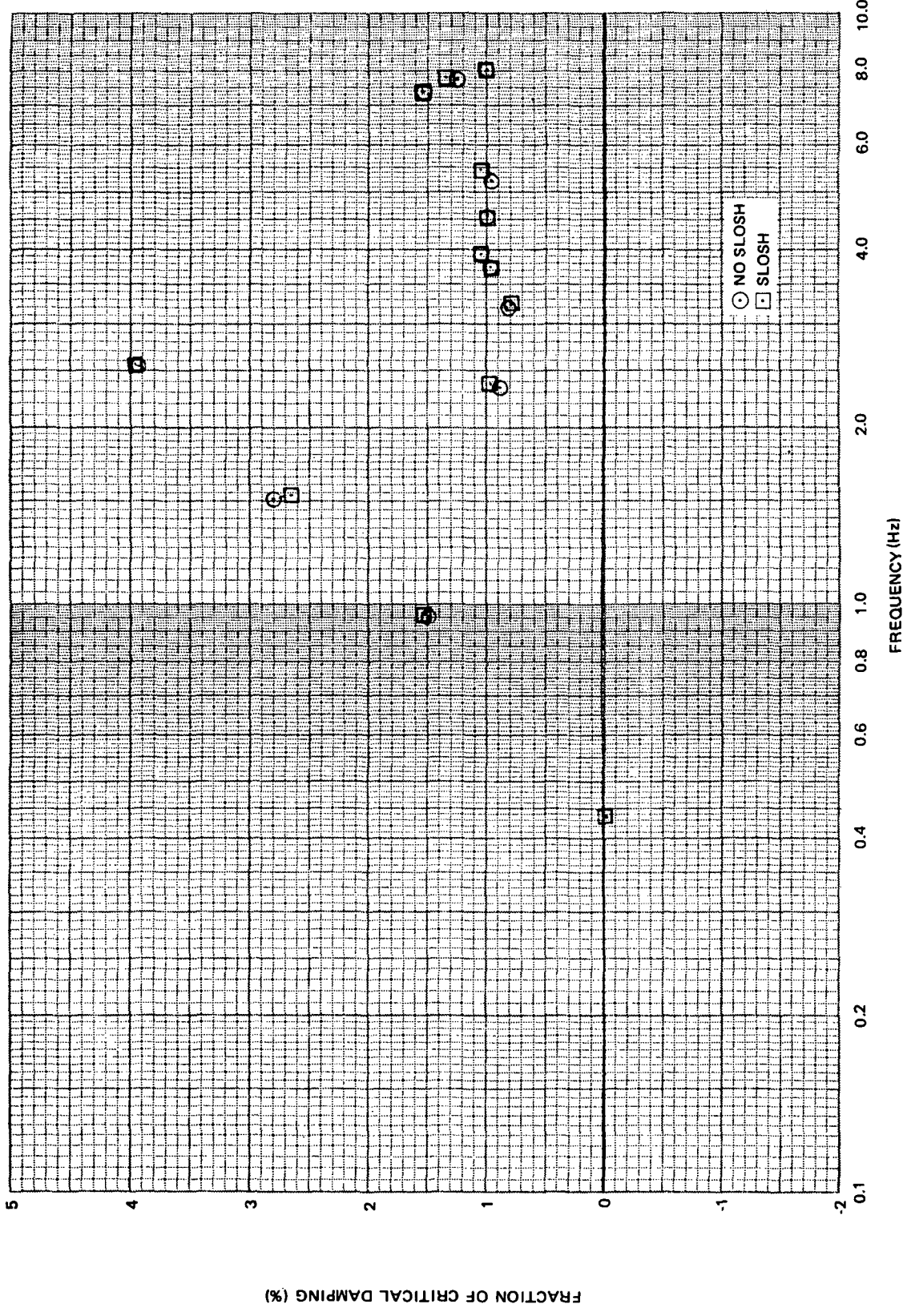


Figure 9. Effect of Slosh on System Roots

The coupled system now had no instabilities. To evaluate the effect of accumulators, the system eigenvalues were computed with the accumulators removed. The system was still stable as illustrated in fig. 10. It therefore appears that with the preliminary engine model, no accumulators would be required. To enhance the pogo participation for this study, subsequent runs were made with no accumulators.

The natural frequencies and those fractions of critical damping differing significantly from the input values of one percent are presented as a function of burn time in fig. 11 and 12, respectively. The lines trace a system eigenvalue, and the test point symbols identify the predominant input mode in the system eigenvector. The effect of the control system is most pronounced at 25 percent burn, which was therefore selected for the baseline.

The preliminary version of the coupled system included 18 structural (to 15.2 Hz) and 12 feedline (to 44 Hz) modes. To improve computational efficiency, this was reduced to 14 structural (to 9.8 Hz) and two feedline (to 7.4 Hz) modes. The resulting eigenvalues were compared with the more complete set. Both frequency and damping were found to be the same within an error of 2 percent. The reduced set of modes was therefore used in all subsequent calculations.

The baseline system was 25 percent burn time with no slosh and no accumulators. The system eigenvalues are presented in fig. 13 for the coupled system and for the pogo and control systems individually. As expected, the coupled system deviation from the input one percent damping is closely approximated by the sum of the individual system deviations. A numerical calculation confirms this: all interaction coefficients were 0.03 or less. Thus the linear approximation is accurate to within three percent (0.03 percent error in fraction of critical damping) for the baseline system.

Sensitivity

It is recognized that the Space Shuttle configuration and the input parameters are preliminary in nature. Reasonable variations were made to the input parameters to investigate both the stability and the interaction. Parametric variations were made to engine gain and damping, control gain and frequency, feedline and structural damping and gain, and structural and feedline frequencies.

As previously noted, a pump inlet pressure perturbation does not produce a net positive gimbal force for this engine, although it does for other candidate Space Shuttle engines. Typical gains (P_C/P_S) for other engines are three to five times greater than the preliminary values for this engine. The coupled system damping is plotted as a function of engine gains from one to ten times nominal in fig. 14. The second feedline mode becomes unstable, i.e., pogos, at a little over five times the nominal gain. This indicates accumulators may be required if the engine performs more typically than preliminary models indicate. The coupled system damping for engine dampings

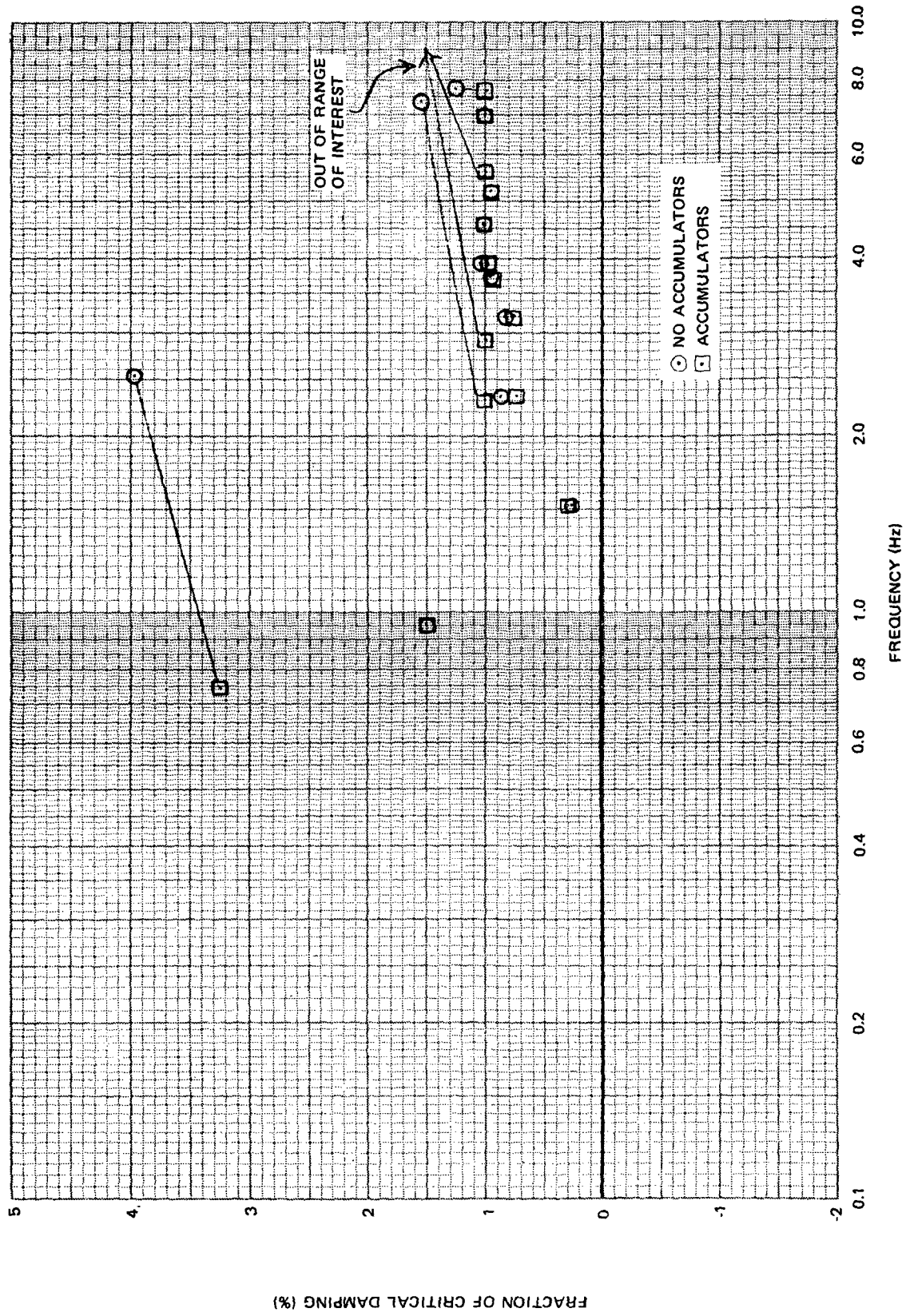


Figure 10. Effect of Feedline Accumulators on System Roots

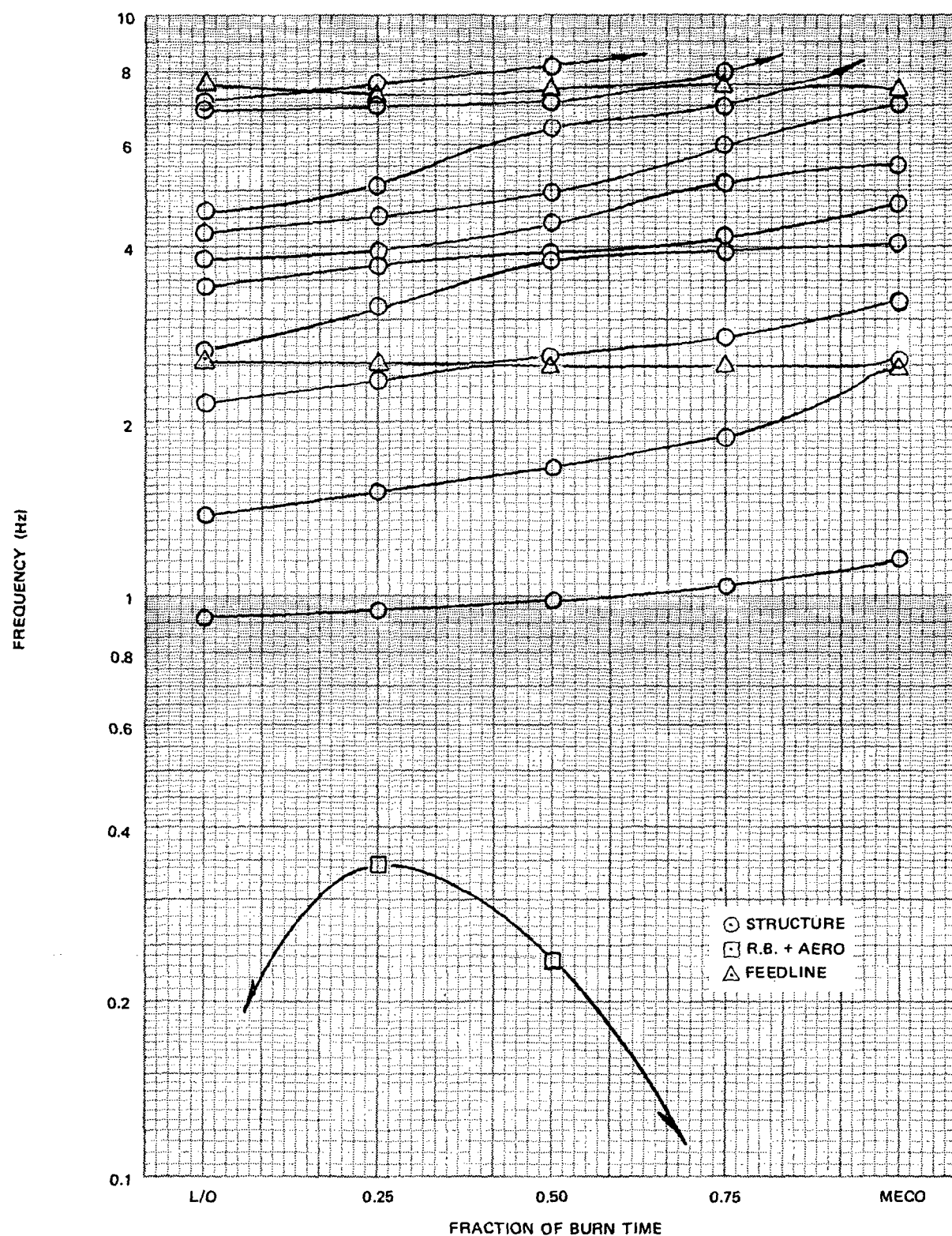


Figure 11. Coupled System Frequencies Versus Burn Time

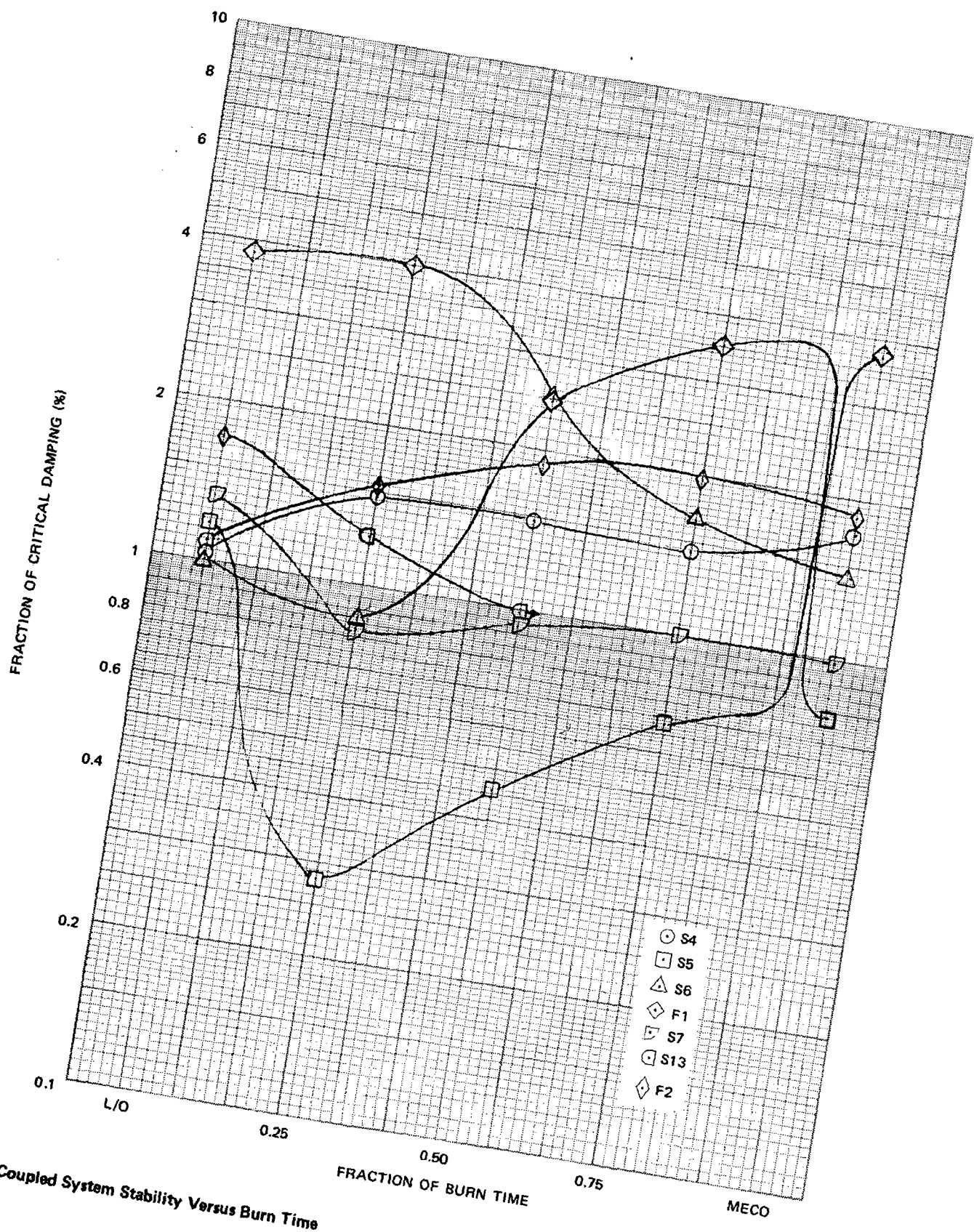


Figure 12. Coupled System Stability Versus Burn Time

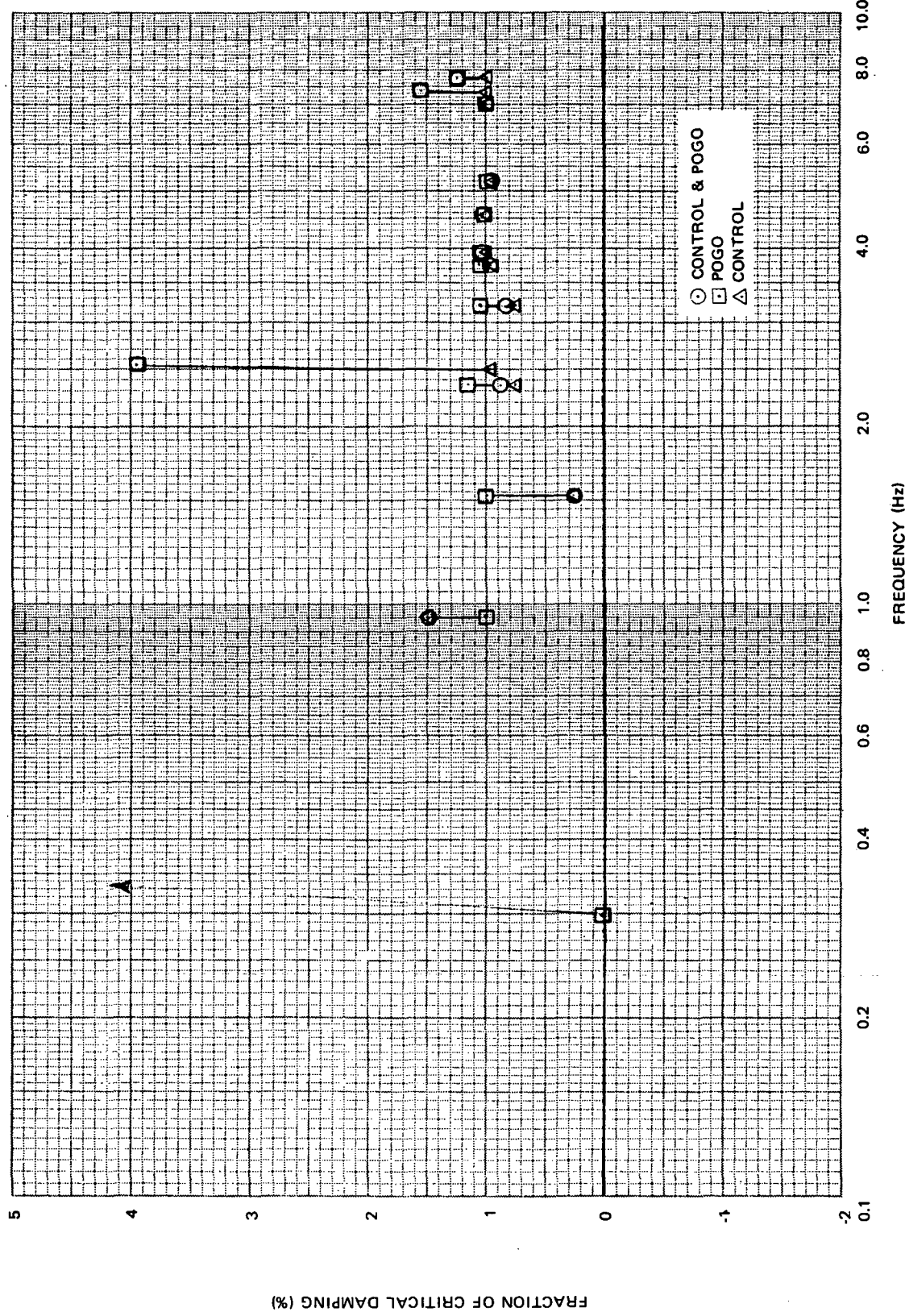


Figure 13. Coupled Versus Uncoupled System Roots

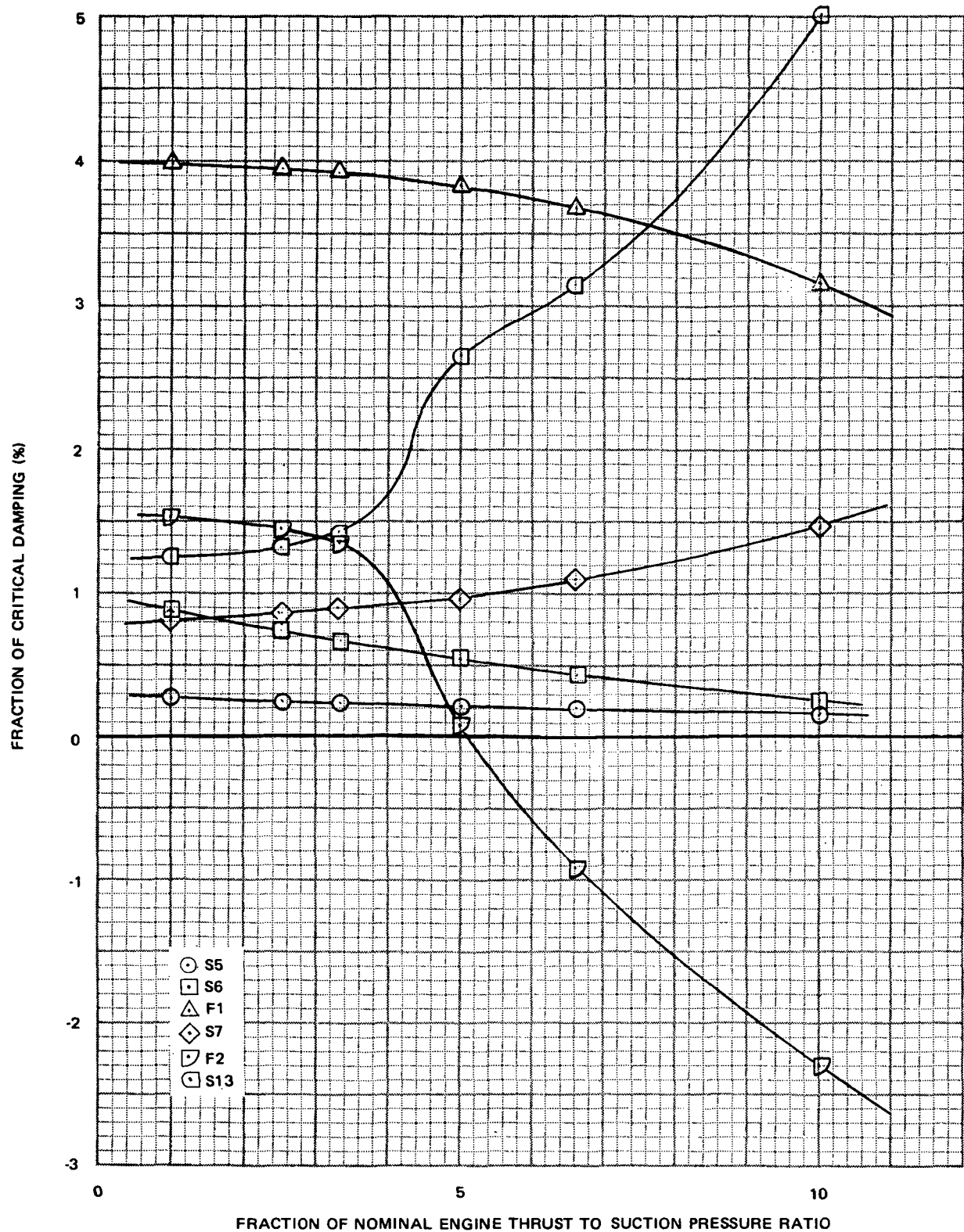


Figure 14. Coupled System Stability Versus Engine Gain

from 0.1 to 10 times nominal are presented in fig. 15. The primary effect of engine damping is to increase the damping in the first feedline mode, thus reducing the likelihood of pogo. The interaction coefficient associated with varied engine models were all at least as small as for the baseline.

The characteristics of the control system are primarily dictated by the gimbal angle feedback loop. Recalling fig. 6 the block has the form:

$$3/(1 + 0.016 s) = X/(1 + \epsilon s)$$

The control system gain is proportional to $1/X$, and the rolloff frequency is proportional to $1/\epsilon$. System damping is presented as a function of control system gain in fig. 16. Reducing the gain substantially reduces the stability of the aero mode, A, (rigid-body pitch) while increasing it reduces the stability of the second flexible mode, S5. Fig. 17 presents system damping as a function of cutoff frequency. Reducing the cutoff frequency tends to destabilize several flexible modes, while increasing it has little effect. It therefore appears that the control system design is adequate. Modifying the control design affects the coupled system in the same way as the control system alone. Stability with respect to control design can therefore be evaluated based on the control system alone. Again, interaction coefficients were almost as small as those for the baseline, producing less than 6 percent error.

The potential for substantial design modification made substantial variations in structural and feedline parameters desirable. The feedline damping was varied from half to twice nominal (see fig. 18). The associated system roots varied correspondingly. Close structural roots were affected in a similar manner but to a lesser extent. Similarly, the structural damping was varied from half to five times nominal. The coupled roots varied correspondingly as illustrated in fig. 19. Reducing structural damping produces a control instability with the second flexible mode, which is normally only 0.27 percent damped due to control coupling. The feedline roots were largely unaffected and therefore not plotted. Interaction coefficients were all at least as small as for the baseline.

The system stability is affected not only by the input damping but by the modal mass of the input modes. The effective modal mass was varied by scaling the mode shapes, and thus altering the modal gain. The effect of varying feedline gain is illustrated in fig. 20. The predominant effect is to enhance the engine damping in the first feedline mode. Other modes are not strongly affected. The interactions remain as small as for the baseline.

The effect of varying structural gain is illustrated in fig. 21. The effect is similar to varying control gain. The aero mode, A, system damping drops with the gain, and the second flexible structural mode, S5, destabilizes as the gain is increased. These effects are due to using a control system which is inappropriate for the modified structural system and would be eliminated in the control design cycle. The first significant interaction, a 21 percent deviation from linearity, occurred at four times the nominal structural

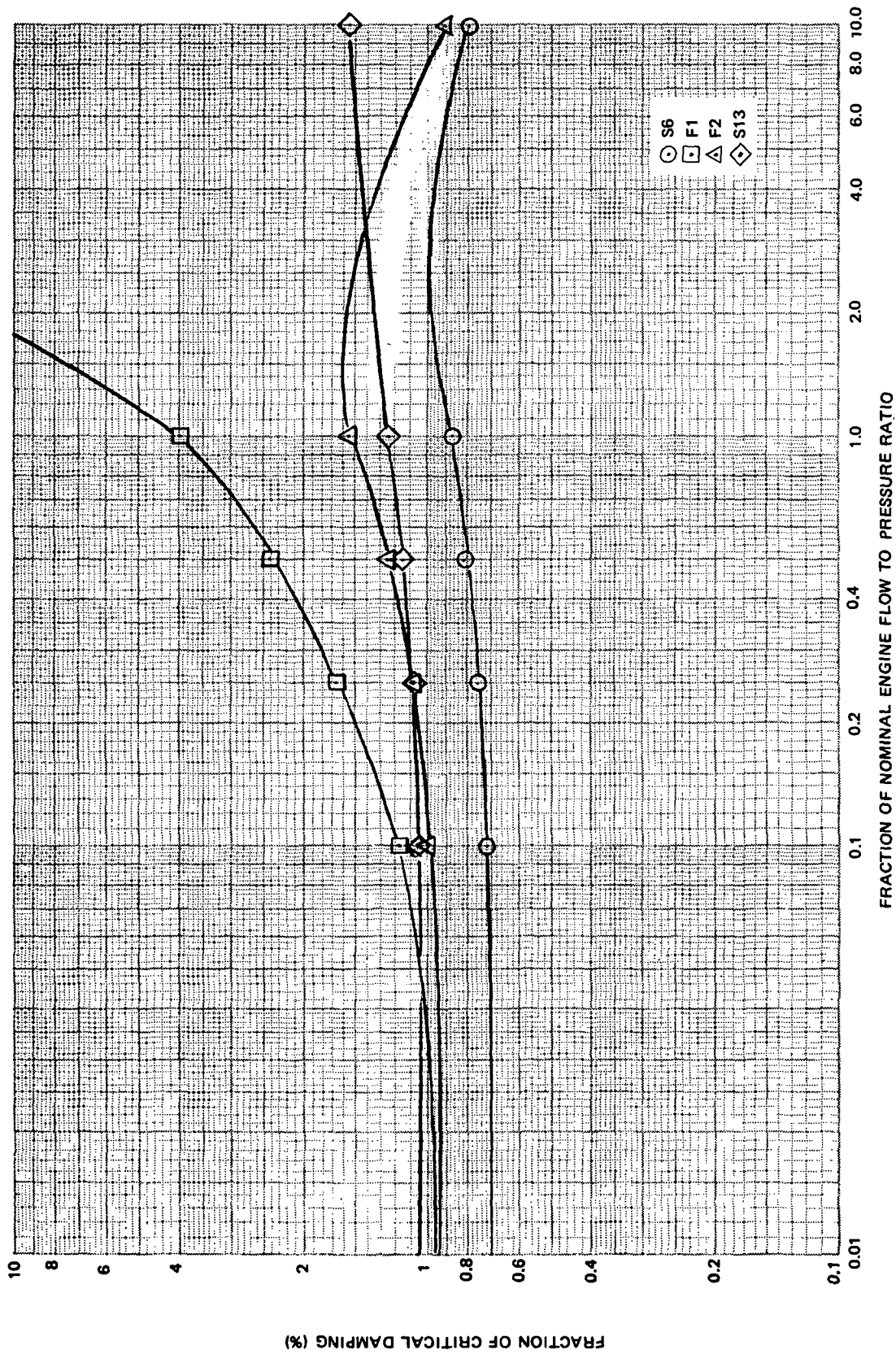


Figure 15. Coupled System Stability Versus Engine Flow

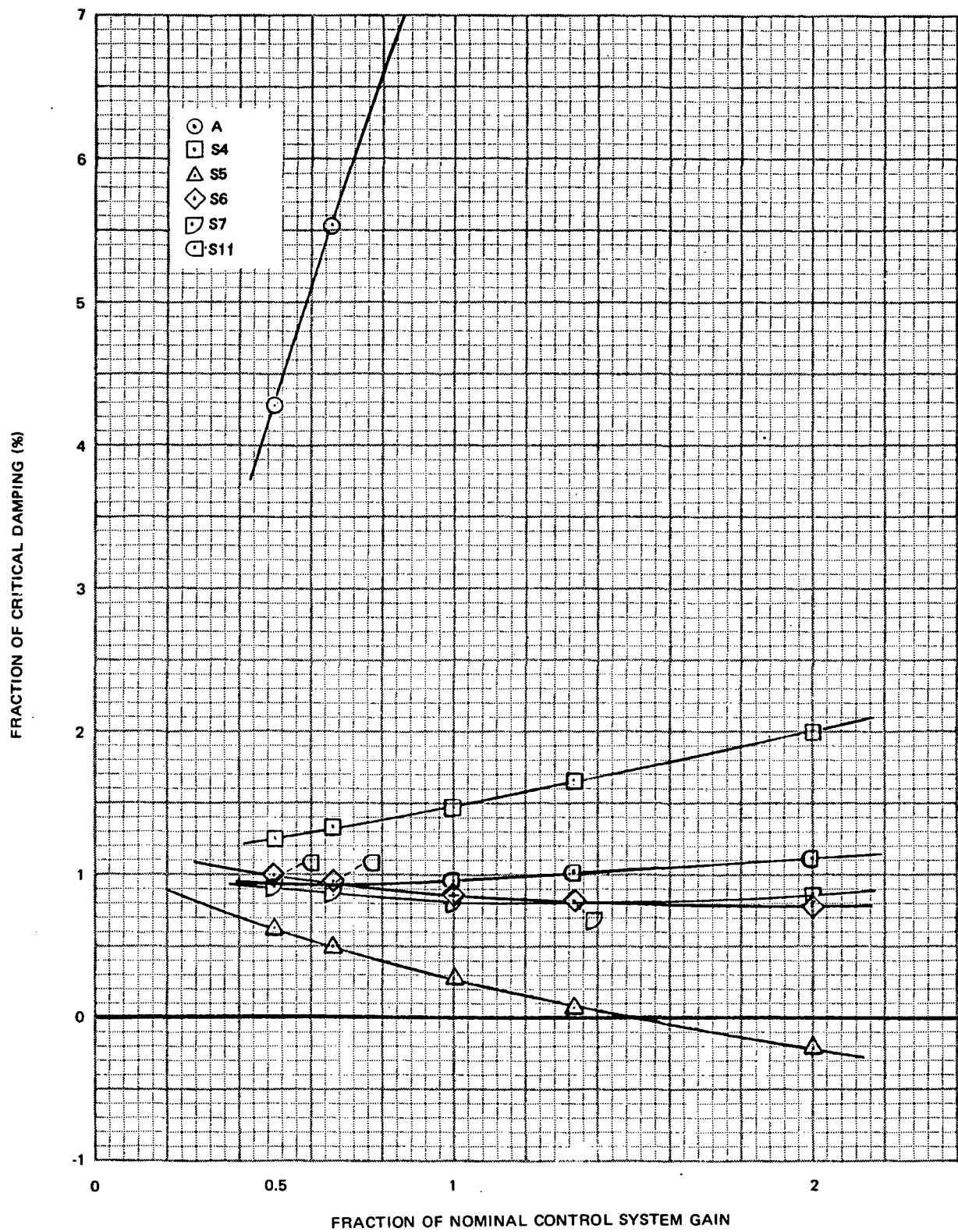


Figure 16. Coupled System Stability Versus Control System Gain

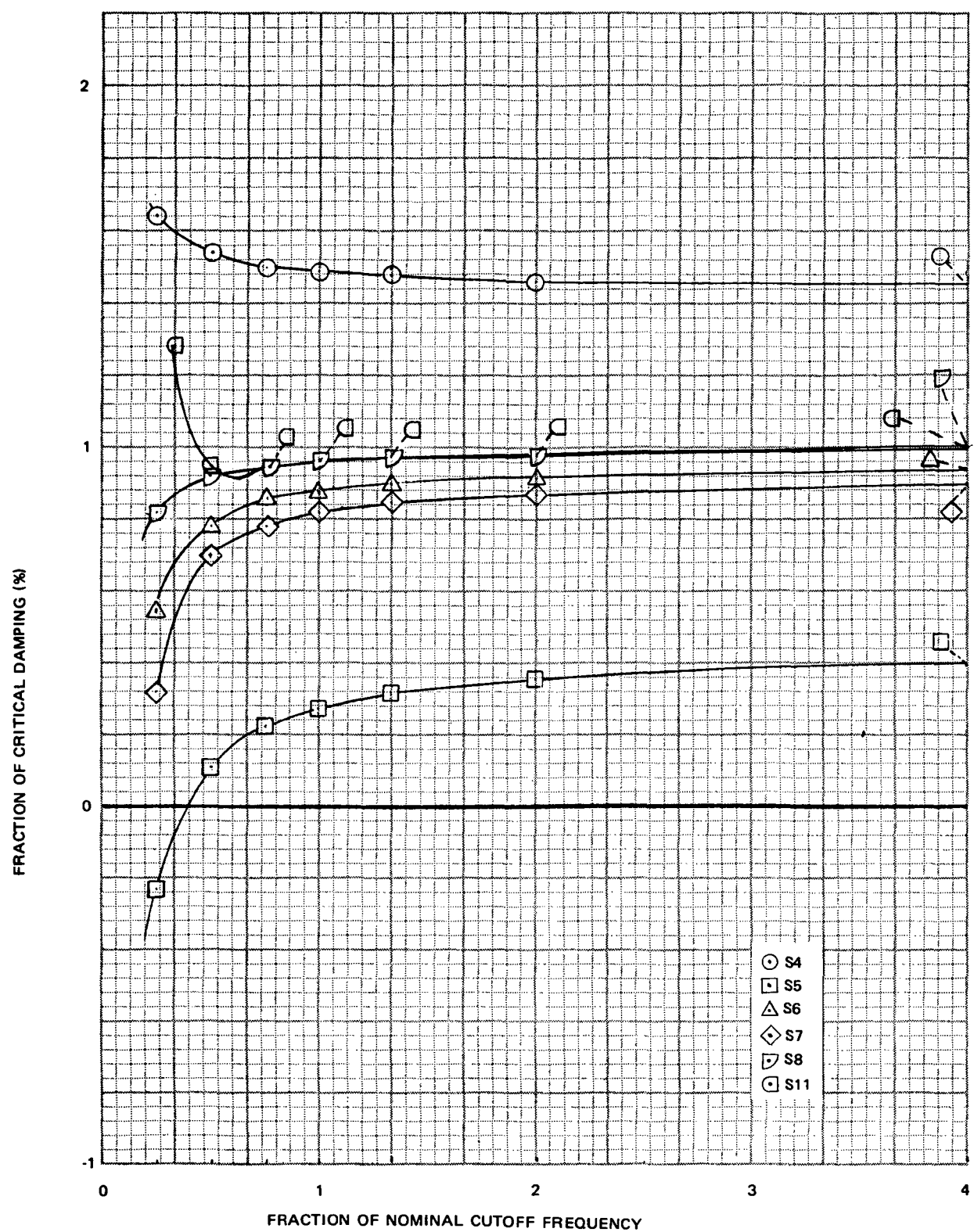


Figure 17. Coupled System Stability Versus Control System Cutoff Frequency

FRACTION OF CRITICAL DAMPING (%)

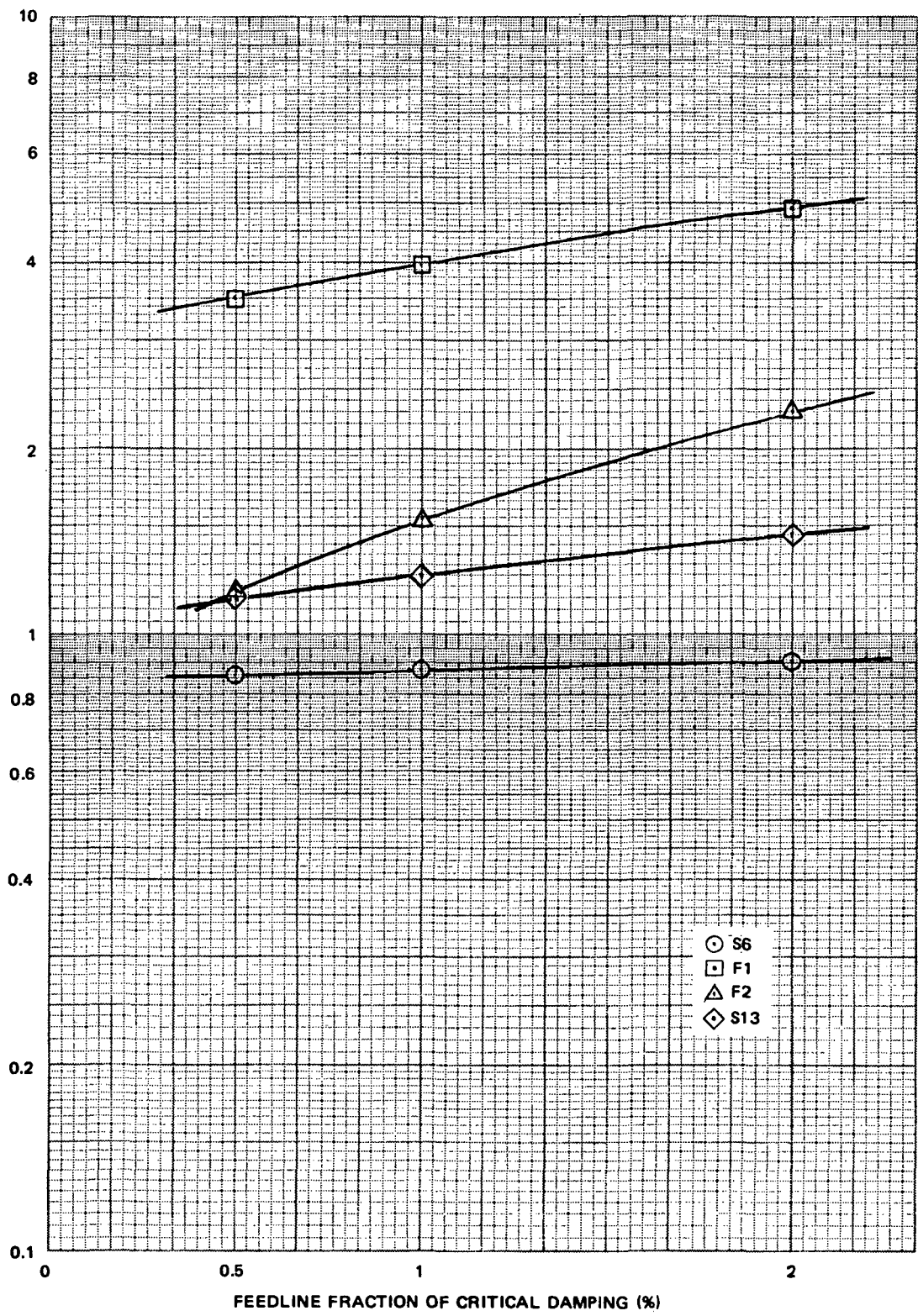


Figure 18. Coupled System Stability Versus Feedline Damping

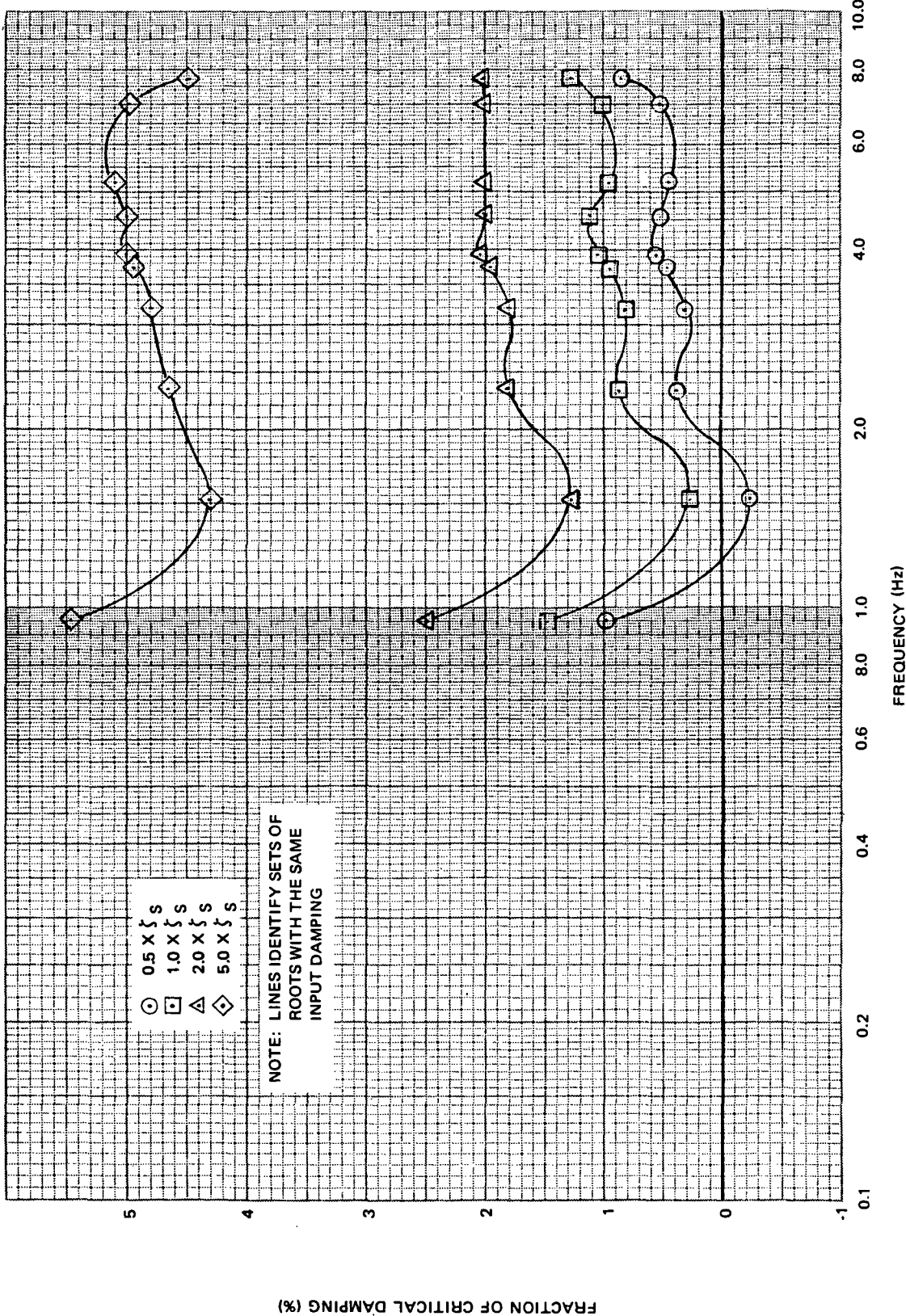


Figure 19. Coupled System Frequencies and Dampings as a Function of Structural Damping

Figure 20. Coupled System Stability Versus Feedline Gain

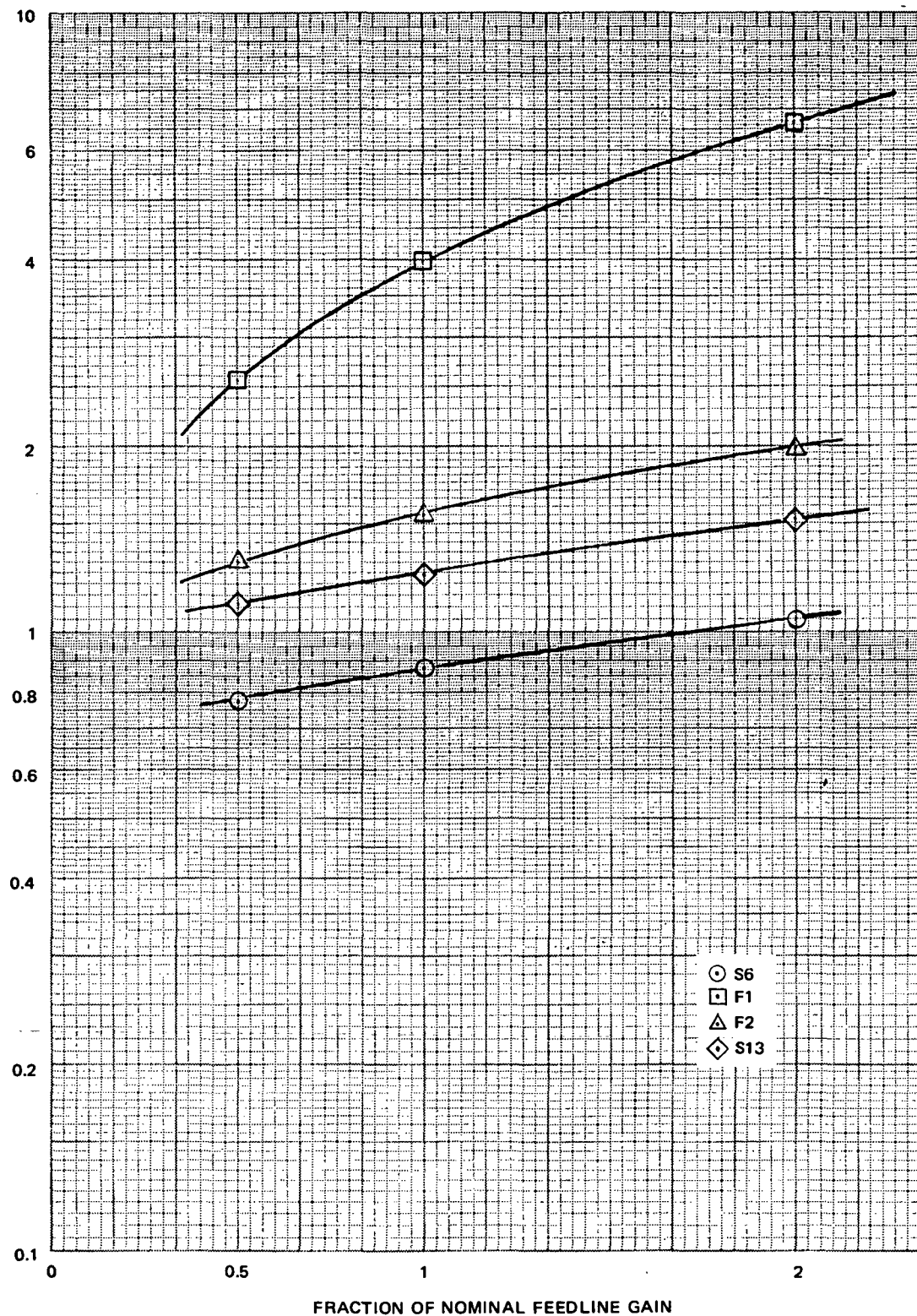


Figure 20. Coupled System Stability Versus Feedline Gain

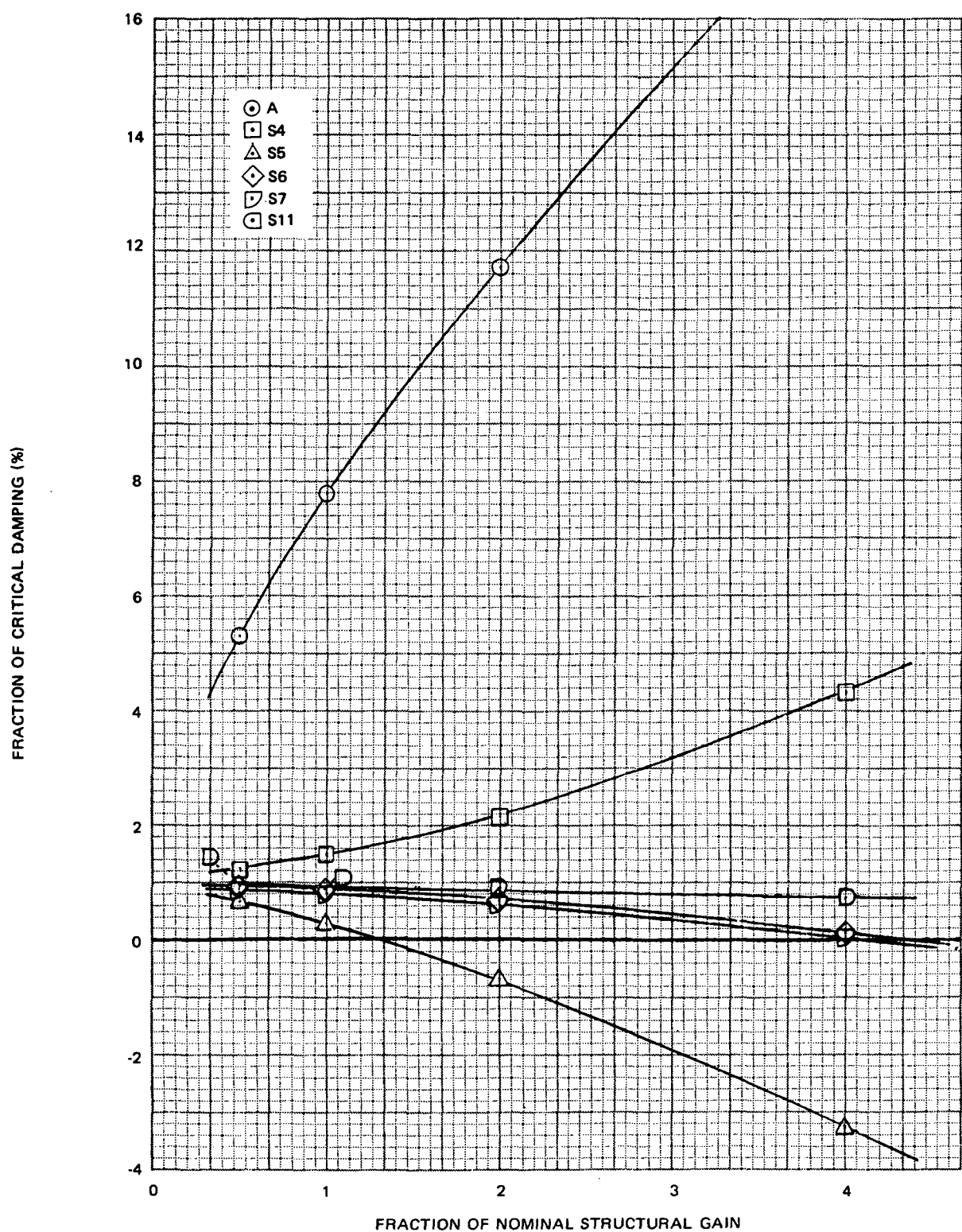


Figure 21. Coupled System Stability Versus Structural Gain

gain in the third flexible structure mode and the first feedline mode. This interaction is attributed to increased coupling between the two modes. The nature of the interaction is best interpreted after examining the sensitivity to shifts in input frequency.

The root behavior when the structural frequencies are scaled is illustrated in fig. 22. A control instability will develop in the eighth flexible mode, S11, as the structural frequencies are decreased. As the frequency drops, the predominantly first feedline root, F1, changes character and becomes predominately the fourth flexible structural mode, S7, and vice versa. In the region of transition, an interaction (not illustrated) of 20 percent occurs in the two modes, S7 and F1. Interaction again occurs only for the strongly coupled modes. The effects of varying the feedline frequency are illustrated in fig. 23. To maximize the interaction, the feedline frequencies were set at structural frequencies; $F_1 = S_5$, S_6 and $F_2 = S_{11}$, S_{12} , S_{13} . The character of several of the system roots changes as the input feedline frequencies sweep through the structural frequencies. As expected, substantial interactions occurred at several points where roots were strongly coupled. A 17 percent interaction was observed at $F_1 = S_5$, and a 50 percent interaction was observed at $F_1 = S_6$.

Two types of instabilities were encountered during the sensitivity investigation. In one the coupled system instability results from a control instability, in the other from a pogo instability. Control instabilities from varying control parameters or structural parameters all occurred when the control system was inappropriate for the associated structure. Pogo instabilities resulting from gains more representative of existing engines would be eliminated by accumulator design. Frequency shifts resulting in strongly coupled, closely spaced roots yielded strong interactions; in all other cases the linear combination of individual dampings was found to be very accurate. To investigate the region of interaction in more detail, the multi-parameter runs described in the next section were made.

Interaction

The nature of the deviation from linearity, which is referred to as interaction, in the region of significant coupling between closely spaced roots was investigated. The root behavior was investigated in detail as the feedline frequency was slowly swept through the structural frequency. The engine model was simultaneously set at four times the gain and one-half of the damping of the nominal engine. This enhances the pogo contribution and makes it more representative of typical engines.

Two regions were investigated in detail, the first and second feedline modes in the vicinity of the second and eighth flexible structural modes respectively. The individual and coupled system root behavior in the vicinity of $F_1 = S_5$ and $F_2 = S_{11}$ are illustrated in fig. 24a and fig. 24b, respectively. Fig. 24a illustrates the fact that a stable control system and a stable pogo system can be combined to produce an unstable coupled system. This instability would be predicted on the basis of a linear combination outside the transition region. It may be noted from the figures that the damping crossing occurs at different

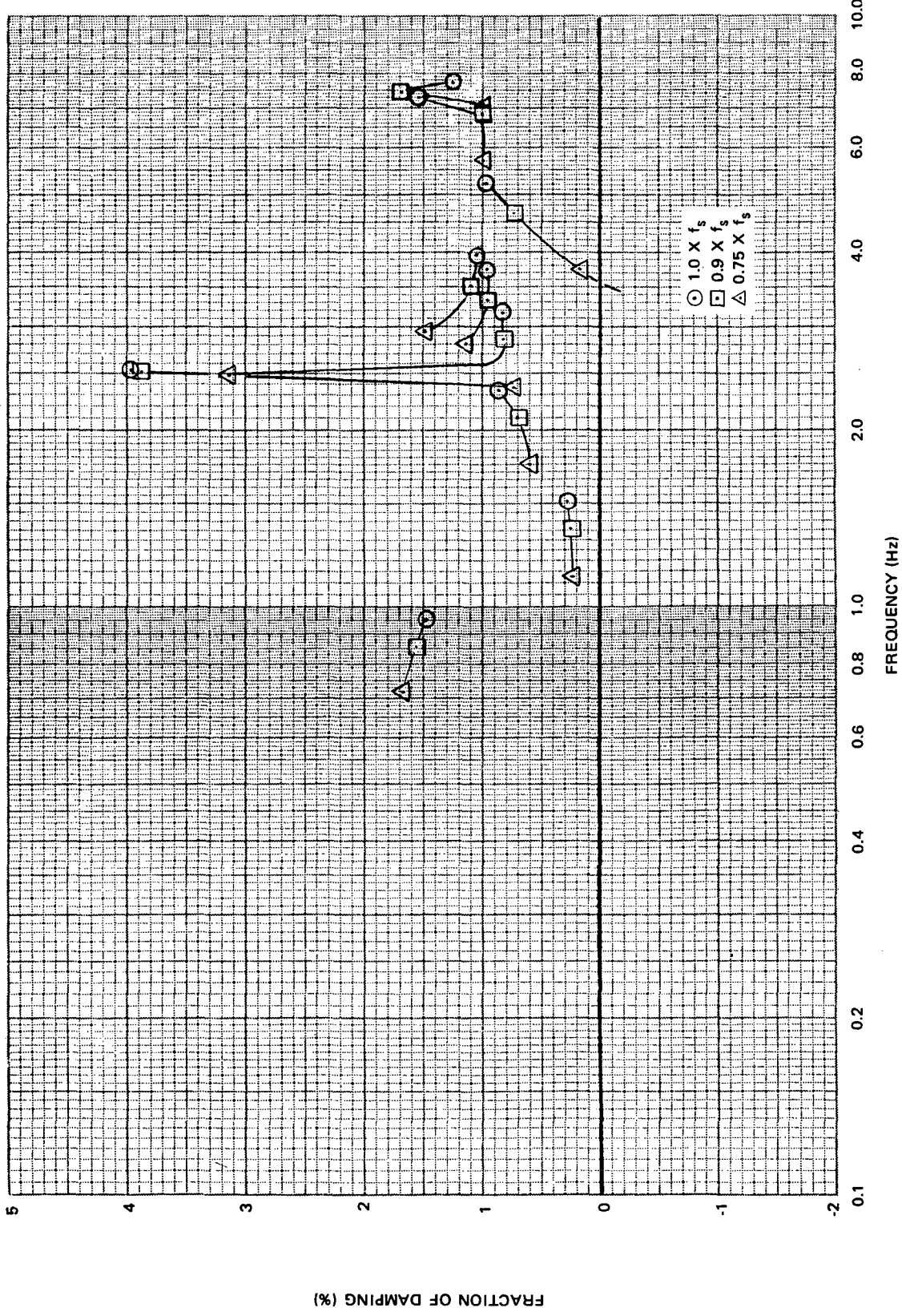


Figure 22. Coupled System Roots as a Function of Structural Frequency

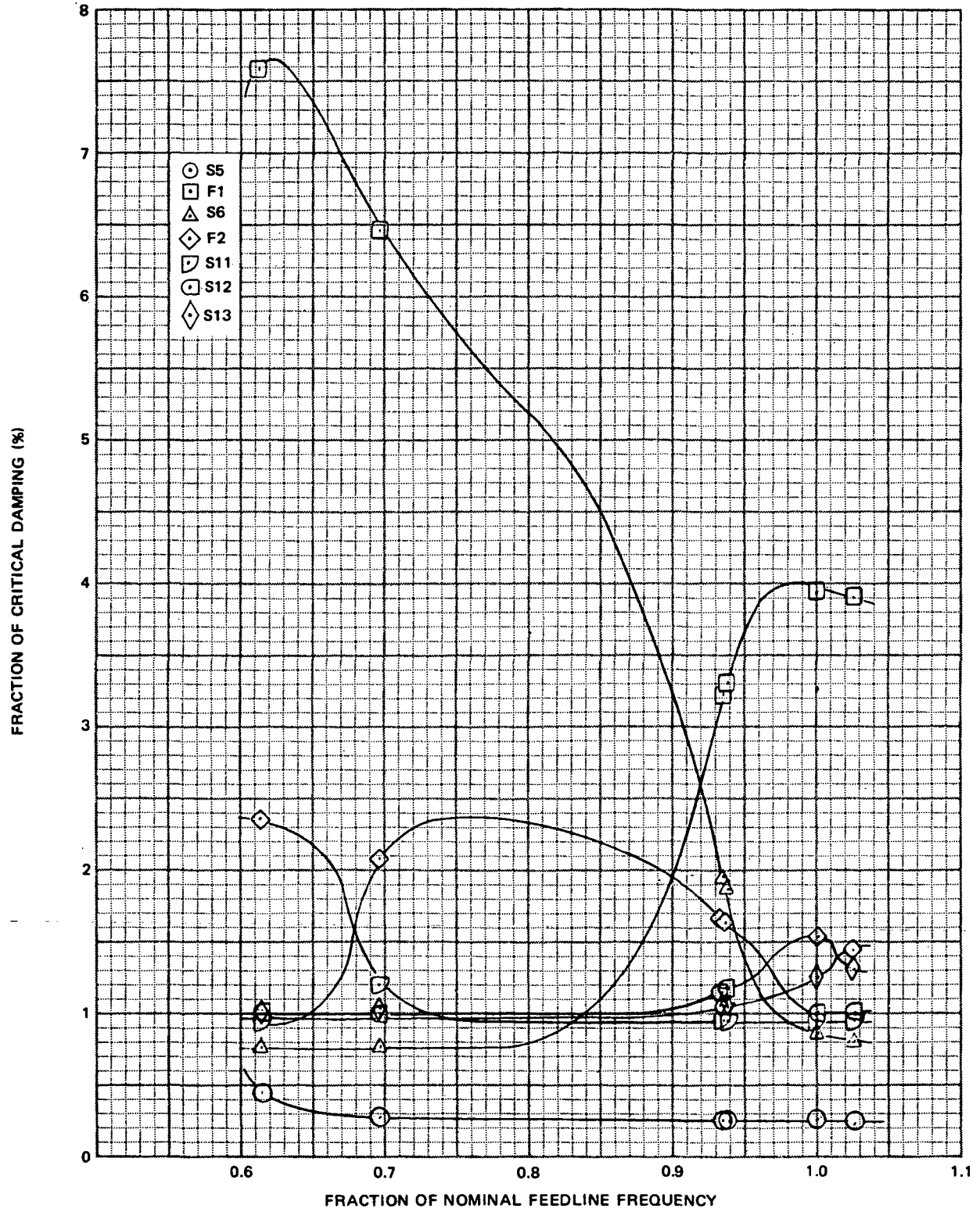


Figure 23. Coupled System Stability Versus Feedline Frequency

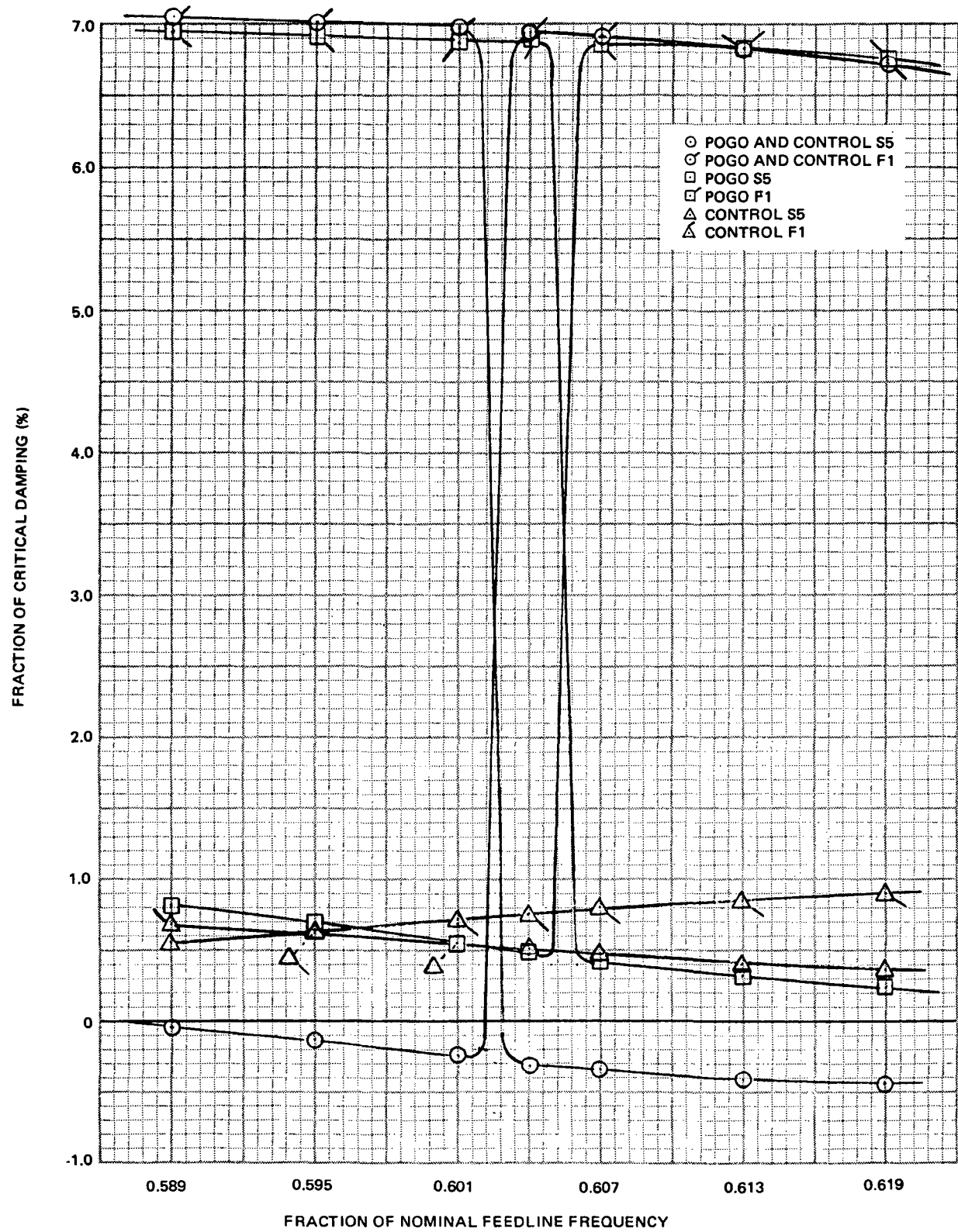


Figure 24A. Coupled and Uncoupled System Stability Versus Feedline Frequency

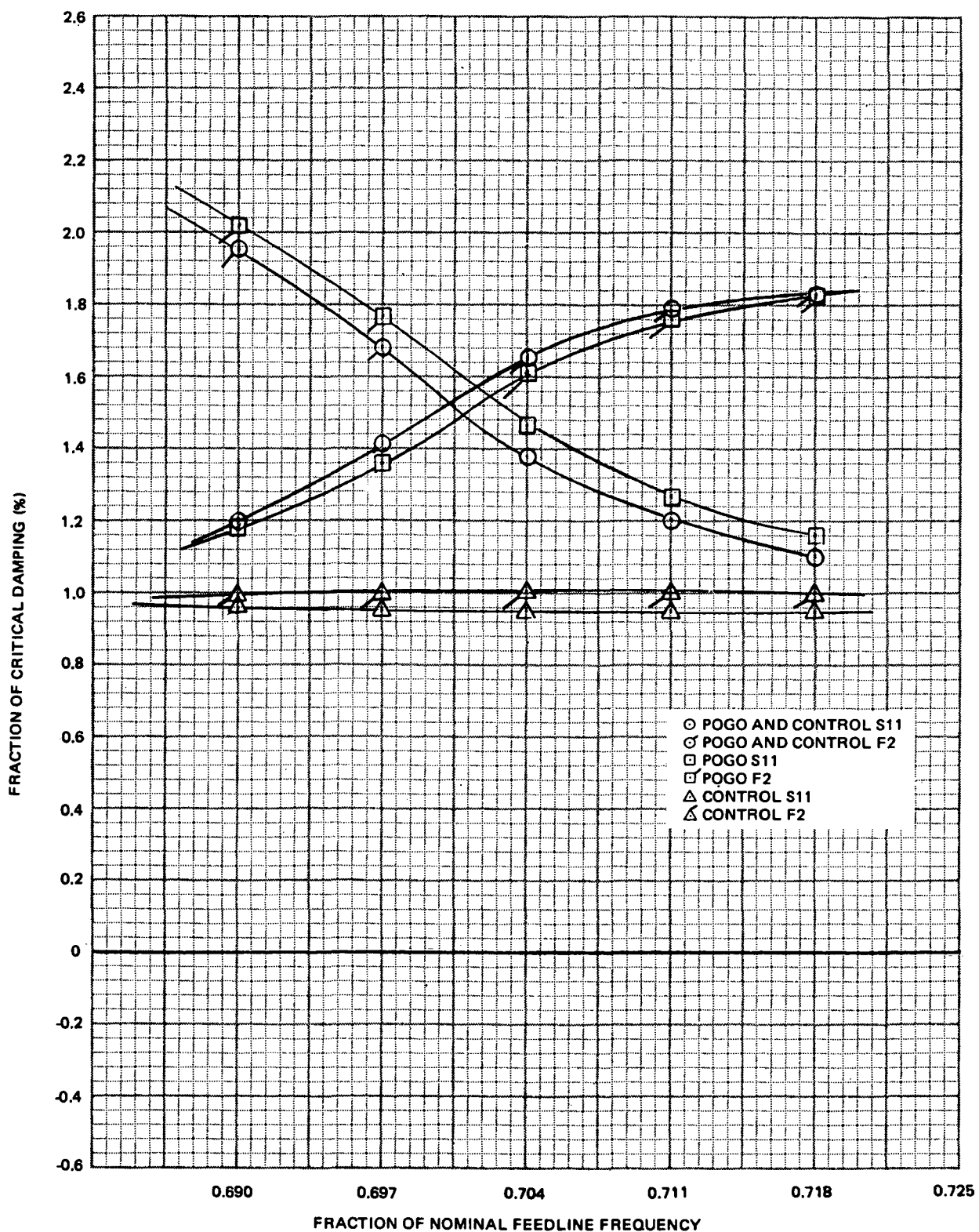


Figure 24B. Coupled and Uncoupled System Stability Versus Feedline Frequency

points for each individual system and for the coupled system. The mode shape for each of the root pairs is undergoing substantial changes in response to small variations in the feedline frequency, moreover the transition is occurring at different input values for each of the individual systems and the coupled system. It is not surprising that the linearity assumption breaks down in that case.

The interaction coefficients associated with fig. 24a are presented in fig. 25. The interactions for the root pair are equal in magnitude but opposite in sign and appear to be correlated with the frequency crossing in the control system, however further study would be required to fully understand the behavior of the interaction coefficients. The linear combination of the envelopes of the separate systems gives the envelope of the coupled system roots. The envelope of the root behavior is meant to imply the smooth curve extrapolated from the region on either side of the associated root crossing. Fig. 26 illustrates the extrapolated control and pogo system curves and the linear prediction for the coupled system. The actual coupled root behavior is depicted by the broken line.

CONCLUSIONS

The nature of the pogo-control interaction was investigated using a coupled structural, feedline, control, and engine system model developed for a representative Space Shuttle. To evaluate the sensitivity of the interaction and stability to design modification, the model was subjected to substantial parametric variations. The stability of each system was determined by closed-loop eigenvalue analysis for four conditions: engine system only active, control system only active, both engine and control systems active, and neither engine nor control system active. Based on these investigations, the following conclusions may be made about vehicles with substantial asymmetries or lateral feedline runs:

- (1) The coupled pogo-control system may be unstable even though the pogo and control systems are separately stable. Major instabilities may exist even though conventional analysis of both the pogo and control system has shown them to be stable.
- (2) The coupled pogo-control system stability can be evaluated on the basis of the separate stabilities of the pogo and control systems as determined by conventional analysis techniques. Specifically, the coupled pogo-control system fraction of critical damping, ζ_{PC} , for any mode is the sum of the damping with the pogo system only, ζ_P , plus the damping with the control system only, ζ_C , less the structural damping with neither pogo nor control systems, ζ_O .

$$\zeta_{PC} = \zeta_P + \zeta_C - \zeta_O$$

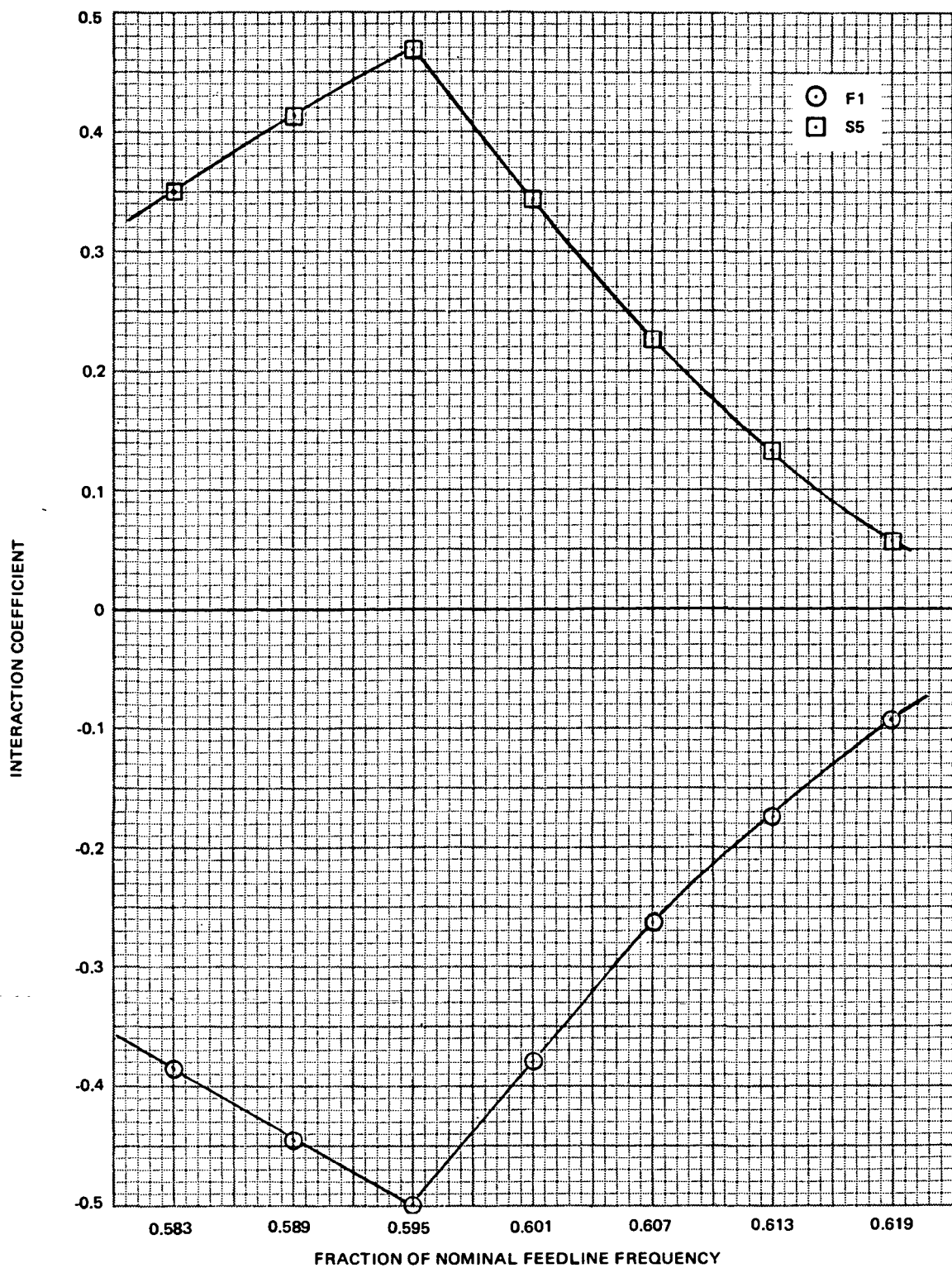


Figure 25. Interaction Coefficient Versus Feedline Frequency

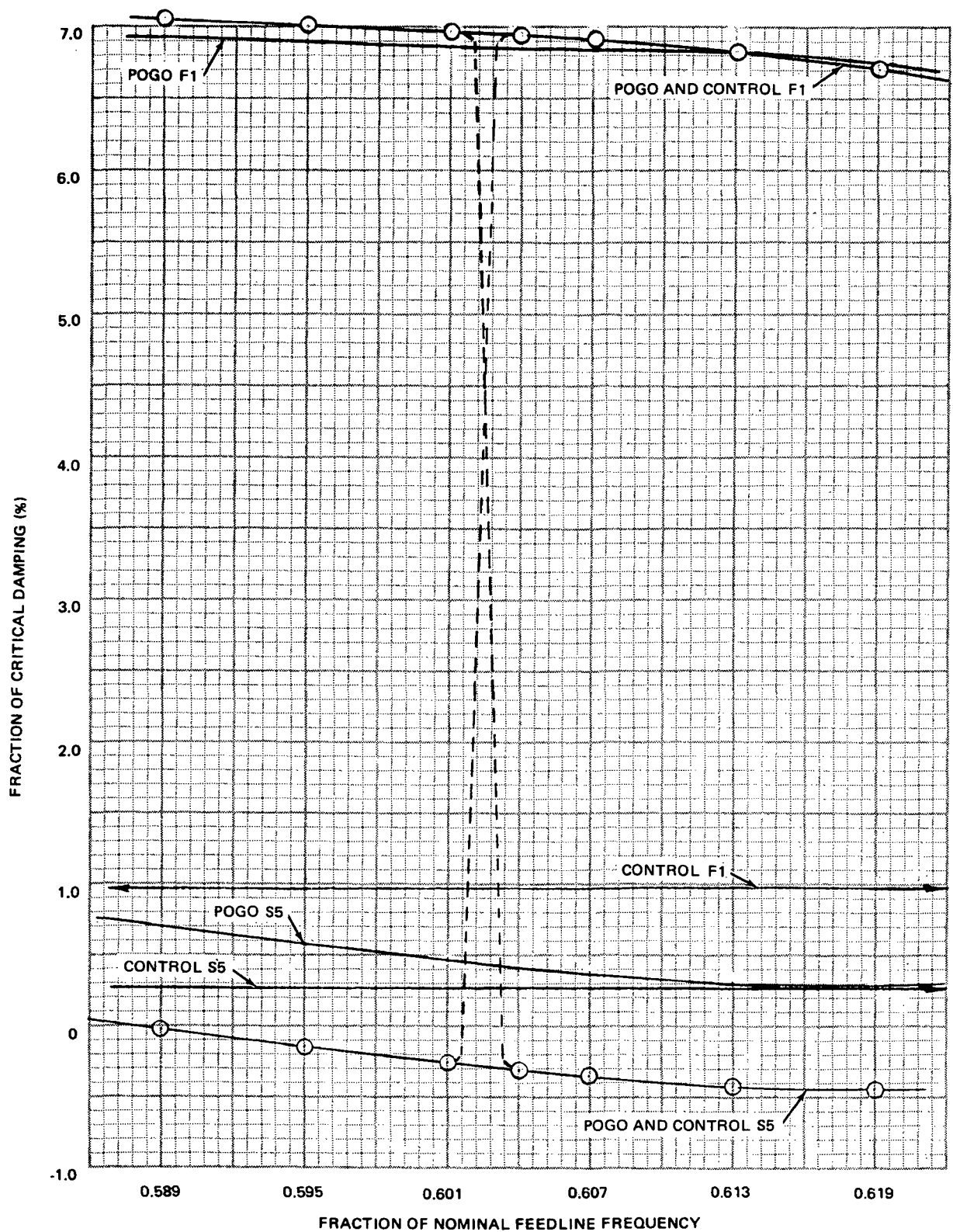


Figure 26. Extrapolated System Stability Versus Feedline Frequency

(3) Although this relationship is imprecise for very close roots, it may be used to predict the upper and lower bounds for the root pair. The individual pogo and control system roots are extrapolated through the region of strong coupling from points outside the region. The upper and lower bounds for the coupled root pair are determined by applying the linear relationship to the extrapolated curves.

On the basis of these conclusions it is evident that pogo-control coupling must be evaluated for vehicles with structural asymmetries or long lateral feedline runs. It is suggested that conventional analysis be performed on the separate pogo and control systems, and that the derived relationship be used to verify the stability of the coupled system. Closed-loop eigenvalue analysis was found to be a very effective technique, and is recommended for future stability investigations. Although the understanding of interaction is incomplete, enough insight has been gained to be used effectively in the design process. It is therefore recommended that future effort be concentrated in the less well understood aspects of pogo such as asymmetric tank dynamics and engine dynamics.

McDonnell Douglas Astronautics Company,
Huntington Beach, California,
May 9, 1972

NATIONAL AERONAUTICS AND SPACE ADMINISTRATION
WASHINGTON, D.C. 20546

OFFICIAL BUSINESS
PENALTY FOR PRIVATE USE \$300

FIRST CLASS MAIL

POSTAGE AND FEES PAID
NATIONAL AERONAUTICS AND
SPACE ADMINISTRATION



NASA 451

"The aeronautical and space activities of the United States shall be conducted so as to contribute . . . to the expansion of human knowledge of phenomena in the atmosphere and space. The Administration shall provide for the widest practicable and appropriate dissemination of information concerning its activities and the results thereof."

—NATIONAL AERONAUTICS AND SPACE ACT OF 1958

POSTMASTER: If Undeliverable (Section 158
Postal Manual) Do Not Return

NASA SCIENTIFIC AND TECHNICAL PUBLICATIONS

TECHNICAL REPORTS: Scientific and technical information considered important, complete, and a lasting contribution to existing knowledge.

TECHNICAL NOTES: Information less broad in scope but nevertheless of importance as a contribution to existing knowledge.

TECHNICAL MEMORANDUMS: Information receiving limited distribution because of preliminary data, security classification, or other reasons.

CONTRACTOR REPORTS: Scientific and technical information generated under a NASA contract or grant and considered an important contribution to existing knowledge.

TECHNICAL TRANSLATIONS: Information published in a foreign language considered to merit NASA distribution in English.

SPECIAL PUBLICATIONS: Information derived from or of value to NASA activities. Publications include conference proceedings, monographs, data compilations, handbooks, sourcebooks, and special bibliographies.

TECHNOLOGY UTILIZATION PUBLICATIONS: Information on technology used by NASA that may be of particular interest in commercial and other non-aerospace applications. Publications include Tech Briefs, Technology Utilization Reports and Technology Surveys.

Details on the availability of these publications may be obtained from:

SCIENTIFIC AND TECHNICAL INFORMATION OFFICE

NATIONAL AERONAUTICS AND SPACE ADMINISTRATION

Washington, D.C. 20546